J. Fluid Mech. (2010), *vol.* 649, *pp.* 69–102. © Cambridge University Press 2010
doi:10.1017/S002211200999334X

Gravity current flow past a circular cylinder: forces, wall shear stresses and implications for scour

E. GONZALEZ-JUEZ[1], E. MEIBURG[1]†, T. TOKYAY[2]
AND G. CONSTANTINESCU[2]

[1]Department of Mechanical Engineering, University of California at Santa Barbara, Room 2355, Engineering II Building, Santa Barbara, CA 93106-5070, USA

[2]Department of Civil and Environmental Engineering, University of Iowa, 4105 Seamans Center for the Engineering Arts and Sciences, Iowa City, IA 52242, USA

(Received 14 March 2009; revised 8 November 2009; accepted 9 November 2009)

The flow of compositional gravity currents past circular cylinders mounted above a wall is investigated numerically. Two- and three-dimensional Navier–Stokes simulations are employed to quantify the force load on the cylinder, along with the friction velocity at the bottom wall near the cylinder, for Reynolds numbers in the range of 2000–45 000. While two-dimensional simulations accurately capture the impact stage, they are seen to overpredict the force and friction velocity fluctuations throughout the transient stage. Comparisons between gravity current and constant-density flows past circular cylinders show that the impact and transient stages are unique to gravity current flows. During the quasi-steady stage, on the other hand, the wake structures and the values of the drag, the peak-to-peak lift, the vortex shedding frequency and the friction velocity below the cylinder are comparable.

The friction velocity below the cylinder depends chiefly on the Reynolds number formed with the front velocity and the gap width. The maximum friction velocity at impact is about 60 % larger than during the quasi-steady stage or in a constant-density flow. This raises the possibility of aggressive erosion behaviour at impact, which may occur in a spanwise localized fashion because of the larger friction velocity near the lobes.

1. Introduction

As the offshore oil and gas industry moves towards deeper ocean environments, submarine structures such as oil and gas pipelines become increasingly exposed to less understood hazards, among them gravity and turbidity currents (Dengler & Wilde 1987; Niedoroda *et al.* 2000; Ross *et al.* 2004; Bruschi *et al.* 2006). Such gravity currents form when a heavier fluid propagates into a lighter one in a predominantly horizontal direction (Benjamin 1968; Simpson 1997). When driven by density differences because of concentration variations of liquids, solutes or gases, these currents are referred to as compositional gravity currents. Alternatively, the driving force may be caused by differential particle loading; in this case the currents are called turbidity currents (Meiburg & Kneller 2010).

---

† Email address for correspondence: meiburg@engineering.ucsb.edu

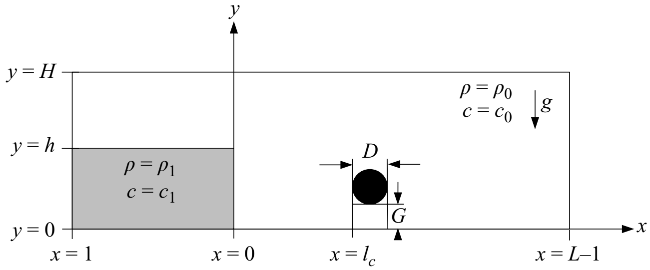

FIGURE 1. Schematic of the flow configuration. A channel of length L and height H contains a lock of length l and height h. When the gate at $x = 0$ is opened, a current of the denser fluid forms and propagates towards a circular cylinder of diameter D, which is situated a distance l_c away from the gate and a distance G above the bottom wall.

Our incomplete understanding of the interaction between gravity currents and submarine structures in the deep sea has motivated several recent experimental (Ermanyuk & Gavrilov 2005*a*,*b*) and numerical (Gonzalez-Juez, Constantinescu & Meiburg 2007; Gonzalez-Juez, Meiburg & Constantinescu 2009*a*,*b*) investigations. These indicate that such flows differ fundamentally from the well-studied problem of constant-density flows past bluff bodies (Williamson 1996; Zdravkovich 1997), because of the presence of a moving front. All of the above-mentioned studies employ the lock-exchange set-up (figure 1), as it allows for the systematic variation of the dominant control parameters. The generic configuration involves a channel of length L and height H, filled with ambient fluid of density ρ_0 and solute concentration c_0. Submerged in it is a lock of length l and height h, which contains a heavier fluid of density ρ_1 and concentration c_1. When the vertical gate at $x = 0$ is opened, the denser fluid forms a compositional gravity current that propagates towards the right along the non-erodible floor of the channel, where it encounters a submerged obstacle after travelling a distance l_c.

Earlier studies based on this configuration have considered both bottom-mounted rectangular cylinders (Ermanyuk & Gavrilov 2005*b*; Gonzalez-Juez *et al.* 2009*a*) and circular cylinders mounted above a wall. For the latter configuration, Ermanyuk & Gavrilov (2005*a*) have discussed experimental measurements of the force acting on the cylinder. Corresponding two-dimensional Navier–Stokes simulations by Gonzalez-Juez *et al.* (2009*b*) investigated the relationship between this force and transient flow structures. As will be discussed below, a number of questions are left unanswered by these two-dimensional calculations, which provides the motivation for the three-dimensional simulation work to be described here. Nevertheless, the two-dimensional simulations by Gonzalez-Juez *et al.* (2009*b*) are able to reproduce the splitting of the current into a portion that flows beneath the cylinder and creates a jet-like flow and another portion that flows over the cylinder. Eventually, the current re-establishes itself further downstream. Both experiments and simulations show that the interaction of the gravity current with the cylinder can be divided into an impact, a transient and a quasi-steady stage. During the impact stage, the drag increases towards a maximum, while the lift undergoes a strong initial fluctuation. The analysis of Gonzalez-Juez *et al.* (2009*a*) has shown that the maximum drag at impact can be up to three times as high as during the quasi-steady stage. For sufficiently wide gaps and large values of the ratio H/h of the channel and lock heights, the two-dimensional simulations show von Kármán vortex shedding during the quasi-steady stage. The shedding frequency and the root mean square (r.m.s.) fluctuations of the lift are close to those for constant-density flows past cylinders near walls. However, in contrast with constant-density flows, the mean lift now has components owing to both buoyancy and the slight deflection of the wake by the denser fluid flow. For wide enough gaps and $H/h = 1$, the shear layer between the dense and light currents is seen to be sufficiently strong and close enough to the cylinder to cancel the roll-up of vorticity, thereby suppressing vortex shedding.

For gravity currents flowing past bottom-mounted square cylinders, Gonzalez-Juez *et al.* (2009*a*) have shown that two-dimensional and three-dimensional simulations produce nearly identical force profiles during the impact stage. However, two-dimensional simulations can notably overpredict the force fluctuations after impact, as a result of more coherent Kelvin–Helmholtz vortices in two dimensions. We note that for the classical problem of constant-density flow past a circular cylinder, Mittal & Balachandar (1995) also found that two-dimensional simulations overpredict the mean drag and r.m.s. fluctuations of the lift in comparison with three-dimensional simulations, as vortices are shed closer to the cylinder in two-dimensional simulations. On the basis of the above observations, our first objective then is to identify the conditions under which results from two-dimensional simulations of gravity current flows past circular cylinders are adequate and when three-dimensional effects become important (§ 3.3). For bottom-mounted square cylinders, the investigation by Gonzalez-Juez *et al.* (2009*a*) sheds some light on the two-dimensional versus three-dimensional issue. However, those results are not directly applicable to the case of a circular cylinder placed some distance above the wall, because of the presence of von Kármán vortex shedding and the effect of the gap.

The three-dimensional simulations of gravity current flows past bottom-mounted rectangular cylinders by Gonzalez-Juez *et al.* (2009*a*) have shown that the gravity current's lobe and cleft structure (Simpson 1997) determines the spanwise variation of the drag at impact. During the quasi-steady stage, a cellular flow structure that is similar to the one seen in constant-density flows dominates (Martinuzzi & Tropea 1993). Hence, our second objective is (*a*) to assess the effect of the lobes and clefts on gravity current flows past circular cylinders mounted some distance above a wall, (*b*) to identify the nature of the three-dimensional flow during the quasi-steady stage and (*c*) to discuss the effect of these three-dimensional flow features on the spanwise variation of the drag (§ 3.4). In addition, we will compare wake flow structure, mean drag and r.m.s. lift fluctuations during the quasi-steady stage for gravity current and constant-density flows past circular cylinders (§§ 3.4 and 3.5). This comparison will provide some guidance as to when the wealth of data for constant-density flows past circular cylinders near walls (Bearman & Zdravkovich 1978; Zdravkovich 1985; Fredsøe & Hansen 1987; Chiew 1991; Lei, Cheng & Kavanagh 1999; Lei *et al.* 2000) is applicable to gravity current flows.

An issue of great concern for flows around pipelines on the seafloor is scour, i.e. the removal of sediment from the vicinity of the pipeline by the flow. Scour represents a threat to the stability of submarine structures, and hence there is great interest in predicting its occurrence. The scour by steady and wavy flows past circular cylinders has been studied extensively in the past (e.g. Whitehouse 1998; Sumer & Fredsøe 2002). Similarly, substantial attention has focused on sediment transport by gravity current flows in the absence of obstacles (e.g. see the reviews by Middleton 1993; Kneller, Bennett & McCaffrey 1999; Meiburg & Kneller 2010; see also the recent high-resolution simulations by Necker *et al.* 2002, 2005; Blanchette *et al.* 2005). However, we are unaware of any fundamental investigation into scour by gravity current flows past cylinders. Hence, our third objective is to take a first step in this direction.

Sumer & Fredsøe (2002) laid out the key mechanisms behind scour. For a circular cylinder situated on an erodible bed, scour starts when the difference in pressure upstream and downstream of the cylinder exceeds a threshold that depends on the properties of the bed. Once this threshold is surpassed, 'piping' sets in, and the bed underneath the cylinder is washed away. The simulations to be discussed below will allow us to formulate a criterion for the onset of scour when a gravity current flows over a bottom-mounted cylinder. The onset of scour is followed by aggressive sediment transport below the cylinder, called tunnelling erosion and by the somewhat weaker lee-wake erosion downstream of the cylinder.

The total sediment transport rate q_t of the current, in terms of volume of sediment material per unit time and unit width, is composed of a bed load component q_b and a suspended load component q_s (Graf 1984). This sediment transport rate q_t has been modelled as a function of the bed properties and the shear stress magnitude $|\tau_w|$ at the bed. It scales as $q_t \sim (|\tau_w| - |\tau_{cr}|)^n$, where $n \geqslant 1$, and $|\tau_{cr}|$ represents a critical wall shear stress. This scaling relationship suggests that the study of sediment transport in gravity current flows past cylinders should begin with the mechanisms that generate the bed shear stresses. Thus, we quantify the wall shear stresses in gravity current flows past cylinders (§ 4). We will first discuss the temporal evolution of $|\tau_w|$ near the cylinder from a representative three-dimensional simulation (§ 4.2). It will then be shown that two-dimensional and three-dimensional simulations predict similar values of $|\tau_w|$ near the cylinder at impact and during the quasi-steady stage (§ 4.3). On the basis of this finding, we will employ two-dimensional simulations to study the influence of various parameters on the values of $|\tau_w|$ near the cylinder. Finally, we will present qualitative arguments for the evolution of scour in gravity current flows along erodible beds, on the basis of our findings for $|\tau_w|$ in non-erodible beds (§ 6).

2. Computational approach

2.1. *Governing equations*

The simulations are based on the Navier–Stokes equations in the Boussinesq approximation, and they follow the approach outlined by Härtel, Meiburg & Necker (2000*b*) and Ooi, Constantinescu & Weber (2005, 2007*b*, 2009). In the usual way, we introduce the buoyancy velocity

$$u_b = \sqrt{g'h}, \tag{2.1}$$

where the reduced gravity g' is defined as

$$g' = g(\rho_1 - \rho_0)/\rho_0. \tag{2.2}$$

The relationship between density and concentration is assumed to be linear:

$$\rho = \rho_0 + \frac{\rho_1 - \rho_0}{c_1 - c_0}(c - c_0). \tag{2.3}$$

By introducing suitable characteristic quantities, we can define dimensionless variables as

$$t^* = \frac{t}{(h/u_b)}, \quad x_i^* = \frac{x_i}{h}, \quad \boldsymbol{u}_i^* = \frac{\boldsymbol{u}_i}{u_b}, \quad p^* = \frac{p}{\rho_0 u_b^2}, \quad c^* = \frac{c - c_0}{c_1 - c_0}. \tag{2.4}$$

As a basis for large-eddy simulations (LESs) with subgrid-scale contributions to the diffusion of momentum and concentration, we thus obtain the governing dimensionless equations for the conservation of mass, momentum and concentration in the form

$$\frac{\partial \boldsymbol{u}_j^*}{\partial x_j^*} = 0, \tag{2.5}$$

$$\frac{\partial \boldsymbol{u}_i^*}{\partial t^*} + \frac{\partial \boldsymbol{u}_i^* \boldsymbol{u}_j^*}{\partial x_j^*} = -\frac{\partial p^*}{\partial x_i^*} + \frac{\partial}{\partial x_j^*}\left(\left(\frac{1}{Re} + \nu_{SGS}^*\right)\left(\frac{\partial \boldsymbol{u}_i^*}{\partial x_j^*} + \frac{\partial \boldsymbol{u}_j^*}{\partial x_i^*}\right)\right) + c^* \, \boldsymbol{e}_i^g, \tag{2.6}$$

$$\frac{\partial c^*}{\partial t^*} + \frac{\partial c^* \boldsymbol{u}_j^*}{\partial x_j^*} = \frac{\partial}{\partial x_j^*}\left(\left(\frac{1}{Re\ Sc} + \kappa_{SGS}^*\right)\frac{\partial c^*}{\partial x_j^*}\right). \tag{2.7}$$

Here $\boldsymbol{u}_i^*$ denotes the velocity vector, p^* the total pressure, c^* the concentration and $\boldsymbol{e}_i^g$ the unit vector pointing in the direction of gravity. The spatial coordinates are denoted alternatively by (x, y, z) or by (x_1, x_2, x_3). As governing dimensionless parameters in (2.5)–(2.7) we identify the Reynolds and Schmidt numbers, respectively, as follows:

$$Re = \frac{u_b h}{\nu}, \qquad Sc = \frac{\nu}{\kappa}, \tag{2.8}$$

where ν represents the kinematic viscosity and κ the molecular diffusivity. A Reynolds number based on the cylinder diameter D and the velocity U to which the cylinder is exposed (to be defined later) is also used throughout the present work and is given by $Re_D = UD/\nu$. In addition, there are various geometrical parameters, the most important ones being H/h, D/h and G/h.

We remark that in the following discussion, it will generally be advantageous to render time dimensionless by means of the front velocity V of the gravity current, since this will frequently lead to a better collapse of data from different flow fields (Gonzalez-Juez *et al.* 2009*a*). Nevertheless, in deriving the above equations we employ u_b for non-dimensionalizing time, since this quantity is known *a priori*, whereas V can be determined only in the course of carrying out the numerical experiment. For the same reason, the lock height h is taken as the length scale, rather than the gravity current height. We note that the height of lock-exchange currents usually is close to $h/2$ (Shin, Dalziel & Linden 2004).

In the two-dimensional simulations, all of the scales of motion are resolved by choosing a sufficiently fine grid and by setting the subgrid viscosity ν_{SGS}^* and diffusivity κ_{SGS}^* in (2.6) and (2.7) to zero. On the other hand, the three-dimensional simulations employ an LES approach, so that a higher-Reynolds-number regime can be reached. With the LES approach, only the large energy-containing scales are resolved, while the effect of the small unresolved scales on the large scales is modelled by evaluating ν_{SGS}^* and κ_{SGS}^* in (2.6) and (2.7) with the dynamic Smagorinsky model (Germano *et al.* 1991; Lilly 1992). Additional details are provided in Ooi *et al.* (2009) and Pierce (2001).

Unless otherwise stated, the bottom $(y = 0)$ and left $(x = -l)$ boundaries of the computational domain, and the surface of the cylinder, are treated as no-slip walls. The top boundary $(y = H)$ is considered to be a slip wall. A convective boundary condition is employed along the right boundary $(x = L - l)$ of the domain (Pierce 2001). In the three-dimensional simulations, the flow in the spanwise z-direction is assumed to be periodic, and three-dimensionality is triggered by means of small random disturbances in the initial conditions (following the approach of Ooi *et al.* 2009).

The flow field is initialized with the fluid at rest everywhere and the dimensionless concentration c^* being one (zero) within (outside) the lock.

2.2. *Numerical methodology*

Equations (2.6) and (2.7) are discretized on a non-equidistant Cartesian mesh and are solved with a finite-volume direct numerical simulation/LES code (Pierce 2001; Pierce & Moin 2004). The velocity components are represented in a staggered fashion with respect to pressure and concentration, in both space and time. All differential operators are discretized using central differences, except for the convection term in the concentration conservation equation (2.7), which is discretized using the QUICK scheme. Time integration is accomplished via an iterative procedure similar to the Crank–Nicolson scheme. To ensure that the continuity equation (2.5) is satisfied, a Poisson equation for the pressure correction is solved at each time step by means of a multi-grid algorithm. The numerical method is second-order accurate in both space and time. The region in the Cartesian mesh where the cylinder is located is decoupled from the fluid via boundary conditions. Inside this region the velocity, pressure and concentration are set to zero. This methodology, called grid blanking, could be considered a simpler form of the immersed boundary technique.

Our code has been validated for the simulation of intrusion currents (Ooi, Constantinescu & Weber 2007*a*), gravity currents over no-slip walls (Ooi *et al.* 2005, 2007*b*, 2009) and gravity current flows past bottom-mounted square cylinders (Gonzalez-Juez *et al.* 2007, 2009*a*), as well as for the simulation of flows past open cavities in which a passive or active scalar is present (Chang, Constantinescu & Park 2006, 2007*a*,*b*) and other types of flows (Pierce 2001; Pierce & Moin 2004). In addition, the predictions of our code for the mean drag, peak-to-peak lift and vortex shedding frequency in two-dimensional flows past square cylinders inside channels are in good agreement with those from recent codes (Gonzalez-Juez & Meiburg 2009).

Since in the present simulation work the circular cylinder is approximated in a Cartesian mesh, we present additional validation data comparing our results with those from other computational investigations of two-dimensional constant-density flows past circular cylinders. The two values of $Re_D = UD/\nu$ considered are 250 and 525, where U is the free-stream velocity. The complete parameters of these two-dimensional simulations can be found in Gonzalez-Juez (2009). Table 1 shows that at $Re_D = 525$ ($Re_D = 250$) the mean drag calculated with our code is within 6 % (2 %); the vortex shedding frequency is within 2 % (1 %); and the peak-to-peak lift is within 5 % (1 %). The level of agreement between our results and those from other investigations is satisfactory for the objectives of the present work. This agreement reflects the fact that the boundary layer on the cylinder is sufficiently thick for the surface roughness not to have a strong influence for the values of Re_D considered here.

2.3. *Parameter range of the simulations*

The length of the computational domain is kept at $L/h = 28$ for all simulations. The width of the domain in the spanwise direction is set to h for the three-dimensional simulations, as is commonly done in experiments (e.g. Simpson 1997; Ermanyuk & Gavrilov 2005*a*,*b*) and simulations (Härtel *et al.* 2000*b*; Cantero *et al.* 2007 and Ooi *et al.* 2009 used a width of $1.5h$). This width should be sufficiently large to resolve the gravity current lobe-and-cleft structure and the flow structures in the cylinder wake. The constant lock length of $l/h = 12$ ensures that during the time of the simulation, reflections from the left wall do not influence the interaction between the gravity current front and the cylinder, so that a constant flux of dense fluid towards the

	$Re_D = 250$		$Re_D = 525$	
Parameter	Posdziech & Grundmann (2007)	Our results	Mittal & Balachandar (1995)	Our results
$F_{D,mean}/(0.5\rho_0 DU^2)$	1.33	1.31	1.44	1.36
$F_{L,pp}/(0.5\rho_0 DU^2)$	1.60	1.62	2.42	2.30
$f/(U/D)$	0.202	0.205	0.210[†]	0.215
L_w/D			0.50	0.50
First separation point			112°	110°
Second separation point			137°	138°

[†]This value is from the experiments by Prasad & Williamson (1997) at $Re_D = 592$.

TABLE 1. Comparison of the results from our simulations and those of others for constant-density flows past circular cylinders at $Re_D = 250$ (Posdziech & Grundmann 2007) and $Re_D = 525$ (Mittal & Balachandar 1995). The quantities considered are as follows: the mean drag $F_{D,mean}/(0.5\rho_0 DU^2)$, peak-to-peak lift $F_{L,pp}/(0.5\rho_0 DU^2)$, vortex shedding frequency $f/(U/D)$ and wake length (L_w/D). Also shown are the location of the first and second separation points behind the cylinder, which can be seen in the mean streamline plots of figure 12 in Mittal & Balachandar (1995); for reference, the stagnation point is at 0°, the top of the cylinder at 90° and the base at 180°.

cylinder is maintained. The ratio of the channel height and the lock height is set to $H/h = 2.5$, which approximates well the deep ambient case of $H/h \rightarrow \infty$ found in practice (Gonzalez-Juez *et al.* 2009*a*). The distance between the gate and the cylinder is set to $l_c/h = 3$ for most simulations, since it ensures that the current is in the constant-front-speed phase (Simpson 1997) when it encounters the cylinder. However, whereas a value of $l_c/h = 3$ is large enough for l_c/h not to be an important parameter of the problem in two-dimensional simulations (Gonzalez-Juez *et al.* 2009*a*), we will see that larger values are needed in three-dimensional simulations; thus, we also consider a value of $l_c/h = 9$ in three-dimensional simulations. Reynolds numbers in the range $Re = 2000$–$45\,000$ are considered, which are typical of laboratory gravity currents. The Schmidt number Sc has a small effect on the dynamics of the flow and is kept at unity (Gonzalez-Juez *et al.* 2009*a*). The ratio of the cylinder diameter and the lock height is $D/h = 0.1$. For comparison, typical gravity current heights O(1–100 m) and cylinder length scales O(1 m) yield a range of $D/h = 0.005$–0.5. A range of gap widths of $G/h = 0.015$–0.15 ($G/D = 0.15$–1.5) is explored, which corresponds to values typically generated through scouring (e.g. Sumer & Fredsøe 2002).

A grid of 1600 × 320 × 60 (1600 × 320) is employed in the three-dimensional (two-dimensional) simulations. The grid is refined near the cylinder to ensure a streamwise and vertical grid spacing of $0.01D$ there. In addition, the grid is also refined near the bottom wall, where the vertical grid spacing is of the order of $0.001h$. With this grid refinement near the wall, the value of the eddy viscosity ν^*_{SGS} at this location is two (one) orders of magnitude less than $1/Re$ in the simulations at $Re = 9000$ ($Re = 45\,000$). The time step size is limited such as to keep the Courant–Friedrichs–Lewy number below a suitable value determined in test simulations. Grid resolution tests were conducted by comparing the results from two-dimensional simulations with grids of 800×160, 1600×320 and 2400×520. Because the results for a grid of 1600×320 were found to be in good agreement with those for 2400×520, the former discretization was selected. For example, the maximum drag at impact, the amplitude

l_c/h	9	3	3	9
Re	9000	9000	9000	45 000
G/h	0.03	0.03	0.15	0.03

TABLE 2. Parameter values employed in the three-dimensional simulations.

of the initial fluctuation of the lift and the maximum wall shear stress right below the cylinder at impact agreed to within less than 1 % for these two grids.

The parameter combinations of the three-dimensional simulations are shown in table 2, and those of further simulations will be discussed later.

3. Force acting on the cylinder

3.1. *Reference case*

The parameters for the reference three-dimensional simulation are $Re = 9000$, $l_c/h = 9$, $D/h = 0.1$ and $G/h = 0.03$; the Reynolds number based on the cylinder's diameter is $Re_D = 459$, as discussed in § 3.5. Figures 2(*a*)–2(*c*) show the temporal evolution of the flow field for the reference case by means of spanwise vorticity isosurfaces, which highlight the interface between the fluids. The cylinder's centre is located at $x/h = 9.05$ for the reference case. Notice in figure 2(*a*) the lobe and cleft structure at the current front (Simpson 1972), as well as the Kelvin–Helmholtz billows further upstream. In figure 2(*b*), the gravity current front has just encountered the cylinder and is now plunging downward immediately downstream of the cylinder. Later on, the current re-establishes itself downstream of the cylinder (cf. figure 2*c*).

Figures 3 and 4(*a*) allow us to associate the temporal evolution of the flow field with the instantaneous force components acting on the cylinder and to define the three stages of the interaction. Here the force exerted by the fluid on the cylinder is calculated by integrating the total pressure around the circumference of the cylinder. The contribution from the shear stresses around the cylinder is negligible for the range of parameters considered (Gonzalez-Juez *et al.* 2007, 2009*a*,*b*). The x and y components of the force are referred to as drag F_D and lift F_L, respectively. They are scaled as $F_D/(0.5\rho_0 DV^2)$ and $F_L/(0.5\rho_0 DV^2)$, while time is normalized as $t/(h/V)$ (Gonzalez-Juez *et al.* 2009*a*). The front speed V of the gravity current is calculated by tracking the foremost point of the $c^* = 0.5$ concentration isosurface. Before the current meets the cylinder, its front speed has a value of $V/u_b = 0.59$ for the reference case ($H/h = 2.5$ and $Re = 9000$), and of $V/u_b = 0.61$ for the high-Reynolds-number case ($H/h = 2.5$ and $Re = 45\,000$). These values compare well with the experimental data of $V/u_b = 0.57$ ($V/u_b = 0.60$) obtained by Shin *et al.* (2004) for $H/h = 2$ ($H/h = 3$).

The drag increases approximately exponentially as the gravity current approaches the cylinder (cf. figure 3*a*), and it reaches a maximum at $t/(h/V) = 9.2$ when the current meets the cylinder (cf. figure 3*b*), marking the end of what we define here as the impact stage. A more detailed analysis shows that the increase of the drag with time is not sensitive to the shape of the cylinder or to the gap distance but is very sensitive to the ratio of the channel height and the lock height. While for $H/h = 1$ the drag increase is almost exactly exponential, it starts to deviate slightly from the exponential form as H/h increases.

During the impact stage the lift undergoes a strong initial fluctuation (cf. figure 4*a*). Notice the formation of a jet of dense fluid in the gap (figures 3*b* and 3*c*) and the

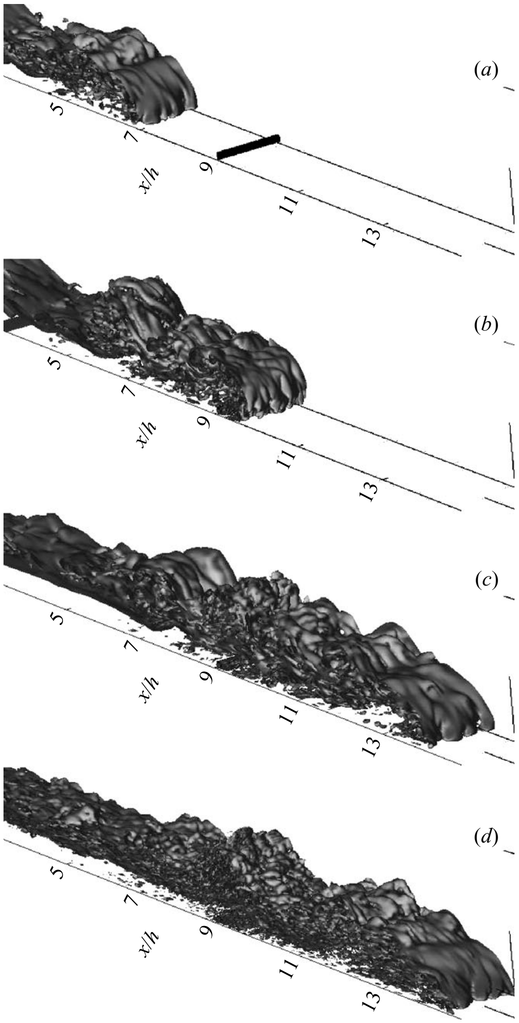

FIGURE 2. Temporal evolution of the gravity current for (*a*–*c*) $Re = 9000$ and (*d*) $Re = 45\,000$. Other parameter values are $D/h = 0.1$, $l_c/h = 9$ and $G/h = 0.03$. Instantaneous spanwise vorticity isosurfaces ($\omega_z/(V/h) = 1$) are shown at $t/(h/V) = $ (*a*) 7.1, (*b*) 10, (*c*) 14.8 and (*d*) 14.6.

later plunge of the head of the current downstream of the cylinder in figure 3(*d*). These two processes are associated with high levels of shear stresses at the bottom wall, as will be seen in § 4. After impact, the drag and lift undergo fluctuations during the transient stage, which ends once these quantities reach a mean quasi-steady value by $t/(h/V) \approx 18$; the so-called quasi-steady stage then begins. We remark that the dimensionless times at which the stages start and end are parameter dependent.

3.2. *High-Reynolds-number case*

A comparison between the reference case ($Re = 9000$, $l_c/h = 9$, and $G/h = 0.03$) and the $Re = 45\,000$ case reveals two important differences. First, note that the spanwise vorticity in the mixing layer between the two fluids and in the cylinder wake takes the form of larger-scale, coherent patches in the reference case (cf. figures 2*c*, 3*e* and 3*f*). On the other hand, these patches are of a much smaller scale, and are much

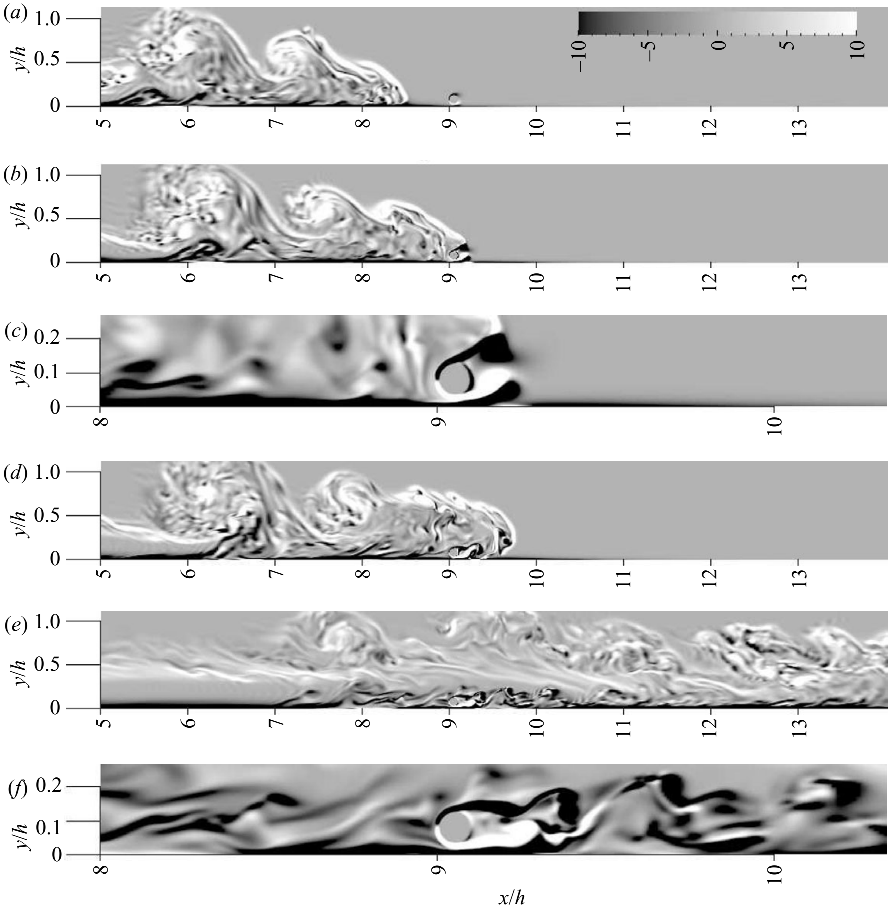

FIGURE 3. Spanwise vorticity $\omega_z/(V/h)$ fields at $z/h = 0.5$ and different times for the reference case $Re = 9000$, $D/h = 0.1$, $l_c/h = 9$ and $G/h = 0.03$: (*a*) $t/(h/V) = 8.5$, (*b*, *c*) $t/(h/V) = 9.2$, (*d*) $t/(h/V) = 9.9$ and (*e*, *f*) $t/(h/V) = 16.3$. The cylinder is located at $x/h = 9$–9.1. The region near the cylinder in (*b*) and (*e*) is enlarged in (*c*) and (*f*), respectively. Note the formation of a jet of dense fluid in the gap in (*b*, *c*) and the later plunge of the current downstream of the cylinder in (*d*). These two processes are associated with high levels of shear stresses at the bottom wall (cf. §4).

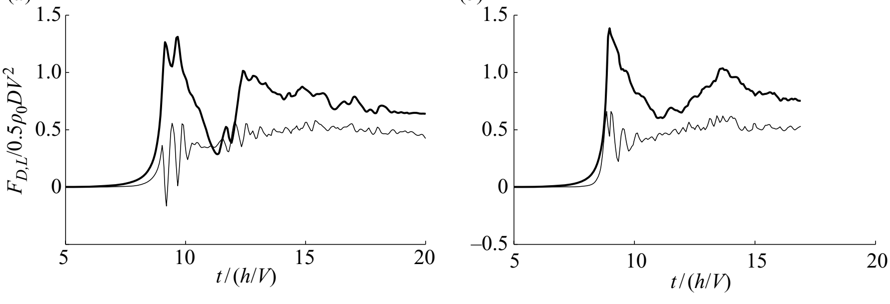

FIGURE 4. Temporal evolution of the spanwise-averaged drag (thick lines) and lift (thin lines) for (*a*) $Re = 9000$ and (*b*) $Re = 45\,000$. Other parameter values are $D/h = 0.1$, $l_c/h = 9$ and $G/h = 0.03$. The lift fluctuation during the impact stage is lower for the higher-Reynolds-number case.

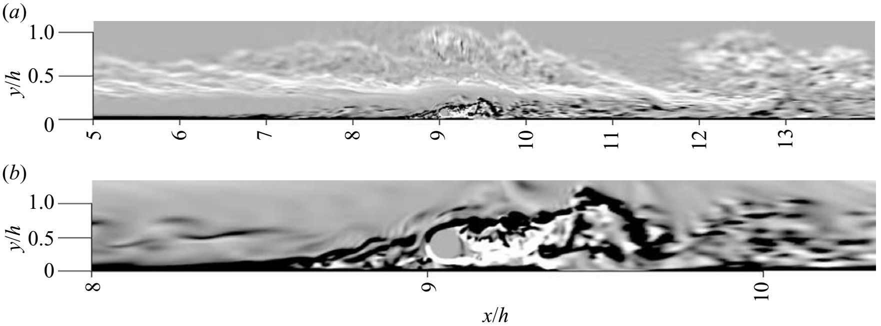

FIGURE 5. Spanwise vorticity $\omega_z/(V/h)$ field at $z/h=0.5$ and $t/(h/V)=16.9$ for $Re=45\,000$, $D/h=0.1$, $l_c/h=9$ and $G/h=0.03$. The cylinder is located at $x/h=9$–9.1. The region near the cylinder is enlarged in (*b*).

more intermittent, in the $Re=45\,000$ case (cf. figures 2*d* and 5). This suggests, from a qualitative standpoint, that these flow regions appear to be laminar or at most weakly turbulent in the reference case and turbulent for $Re=45\,000$. The second important difference between these two cases concerns the stronger initial lift fluctuations in the interval $t/(h/V)=9$–11 for the lower-Re case (cf. figures 4*a* and 4*b*). A key mechanism for generating these fluctuations is the temporal variation of the horizontal velocity difference between locations right above the cylinder, outside the boundary layer and the gap (Gonzalez-Juez *et al.* 2007, 2009*b*). This horizontal velocity difference, which can be related to the lift through Bernoulli's principle, is larger for the lower-Re case, resulting in stronger lift fluctuations.

3.3. *Range of validity of two-dimensional simulations*

Earlier investigations of gravity current flows without submerged cylinders observed the formation and convection of separated flow structures along the bottom wall by the action of the Kelvin–Helmholtz billows at the interface between the two fluids (Härtel *et al.* 2000*b*; Cantero *et al.* 2007). Our recent simulations of gravity current flows past bottom-mounted square cylinders show that these Kelvin–Helmholtz billows and separated structures affect the unsteady force loads after impact (Gonzalez-Juez *et al.* 2009*a*). This effect is more pronounced in two-dimensional than in three-dimensional simulations, since these flow structures are more intense and coherent in two-dimensional simulations. Furthermore, while the effect of these flow structures on the unsteady force load is limited to the transient stage in three-dimensional simulations, it can last much longer in two-dimensional simulations at higher Reynolds numbers $O(10\,000)$, as the three-dimensional breakup because of spanwise instabilities is absent in two-dimensional simulations (Gonzalez-Juez *et al.* 2009*a*). Consequently, the force fluctuations beyond the impact stage are notably overpredicted by two-dimensional simulations at large Re values. Below we will find that for circular cylinders with a gap, even in two-dimensional simulations the effect of these separated structures on the unsteady force load is limited to the transient stage. This represents a key difference between the cases of a circular cylinder with a gap and a bottom-mounted rectangular cylinder.

We begin by focusing on the influence of the distance l_c/h between the gate and the cylinder on the temporal evolution of the flow field and the force loads in three-dimensional simulations. This will be helpful for interpreting the subsequent comparison of two-dimensional and three-dimensional simulation results. For the

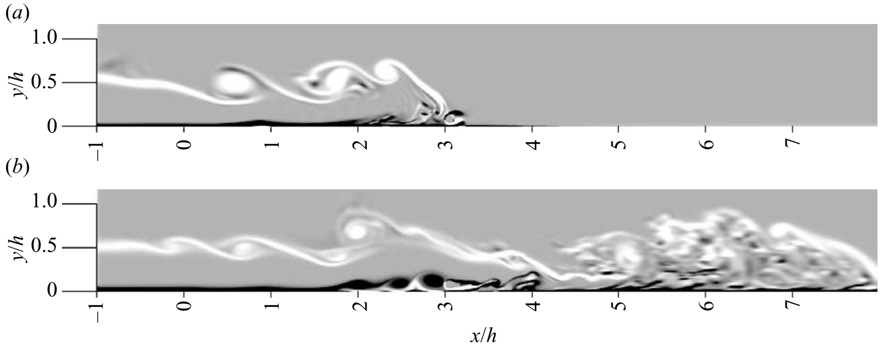

FIGURE 6. Spanwise vorticity $\omega_z/(V/h)$ fields at $z/h=0.5$ and at different times for $Re=9000$, $D/h=0.1$, $l_c/h=3$ and $G/h=0.03$: (*a*) $t/(h/V)=3.2$ and (*b*) $t/(h/V)=8.3$. The cylinder is located at $x/h=3$–3.1, which is too close to the gate to allow for the three-dimensional breakup of the Kelvin–Helmholtz billows. This results in large force fluctuations during the transient stage.

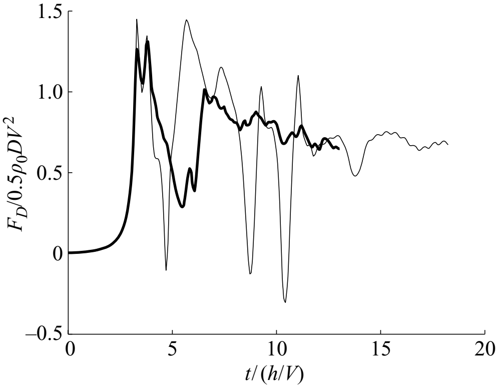

FIGURE 7. Temporal evolution of the spanwise-averaged drag for the reference case $Re=9000$, $D/h=0.1$, $l_c/h=9$ and $G/h=0.03$ (thick solid line) and for the case with the same parameters but a shorter distance $l_c/h=3$ between the gate and the cylinder (thin solid line). The curve for the reference case has been shifted along the abscissa so that the first drag maxima of both cases coincide.

reference case with $l_c/h=9$, the cylinder is located sufficiently far from the gate to allow for the three-dimensional breakup of the Kelvin–Helmholtz billows and their associated recirculation zones along the bottom wall before the current meets the cylinder (cf. figures 3*a*, 3*e* and 3*f*). On the other hand, for $l_c/h=3$, the cylinder is too close to the gate to allow for this breakup, and hence the resulting Kelvin–Helmholtz billows and recirculation zones are still very coherent by the time they encounter the cylinder (cf. figures 6*a* and 6*b*). Consequently, as figure 7 shows, while the drag undergoes only one large fluctuation in the time interval $3.3<t/(h/V)<14$ for the reference case with $l_c/h=9$, it undergoes three large fluctuations in the same time interval for the case with $l_c/h=3$. Note that the curve for the reference case has been shifted along the abscissa in figure 7 in order to have the first drag maxima of both cases coincide. The maximum drag at impact is affected only weakly by this change of l_c/h ($<10\,\%$ change). We can conclude that as long as l_c/h is sufficiently large for the current to reach a constant front velocity and to allow for the three-dimensional

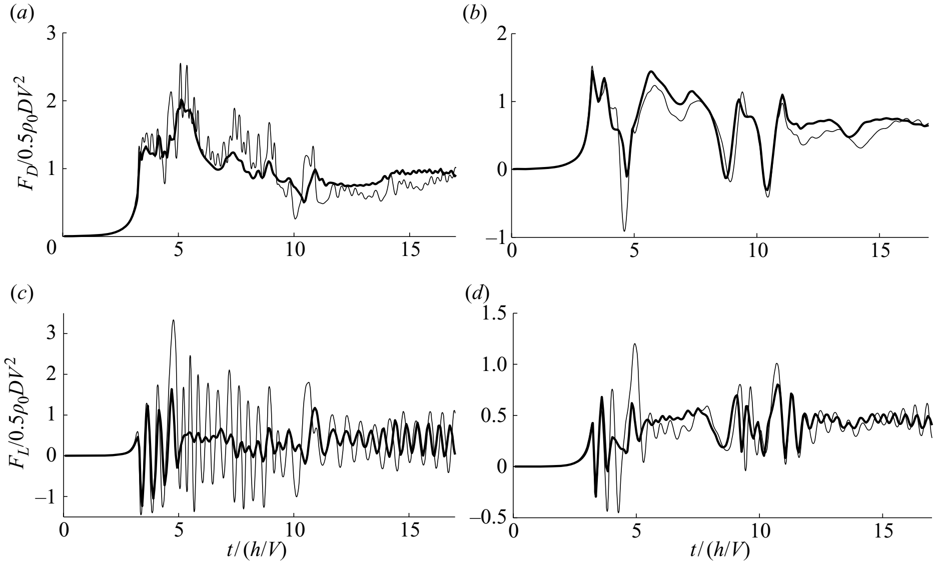

FIGURE 8. Comparison of the spanwise-averaged (a,b) drag and (c,d) lift between two-dimensional (thin lines) and three-dimensional (thick lines) simulations for $Re = 9000$, $D/h = 0.1$, $l_c/h = 3$ and (*a*, *c*) $G/h = 0.15$ and (*b*, *d*) $G/h = 0.03$. Two-dimensional simulations of gravity current flows past circular cylinders provide quantitatively accurate information for the impact stage. During the later flow stages, they capture the correct fluctuation frequency while overpredicting the fluctuation amplitude.

breakup of the Kelvin–Helmholtz billows, this quantity is no longer a dominant parameter.

For the sake of completeness we mention that corresponding two-dimensional simulations (not shown here) show the effect of l_c/h on the force fluctuations during the transient stage to be much less pronounced, as long as the current front has reached a constant velocity by the time it encounters the cylinder.

We now focus on comparing predictions from two-dimensional and three-dimensional simulations for two values of the gap (G/h). For a detailed discussion of the effect of the gap size in two-dimensional simulations, the reader is referred to Gonzalez-Juez *et al.* (2009*b*). For the impact stage $t/(h/V) < 3.3$, figure 8 shows the two-dimensional and three-dimensional simulation results to be in good agreement. For the quasi-steady stage $t/(h/V) > 14$, on the other hand, the amplitude of the force fluctuations is overpredicted by the two-dimensional simulations, while their frequency is accurately captured. Note that the increase of the fluctuation amplitude with G/h is reproduced correctly by the two-dimensional simulations. During this late stage, both two-dimensional and three-dimensional simulations show the presence of von Kármán vortex shedding for the larger gap (cf. figure 9 for the three-dimensional results). Conversely, for the smaller gap only clockwise vortices exist (figure 3), since the vorticity in the cylinder's bottom shear layer is effectively cancelled by the vorticity of opposing sign in the bottom-wall boundary layer (Taniguchi & Miyakoshi 1990; Lei *et al.* 2000; Gonzalez-Juez *et al.* 2009*b*). Neither two-dimensional nor three-dimensional simulations show the convection of separated flow structures along the bottom wall upstream of the cylinder during the quasi-steady stage, for the present parameters. Hence the observed overprediction of the force fluctuations during the quasi-steady stage by two-dimensional simulations is not due to overly coherent

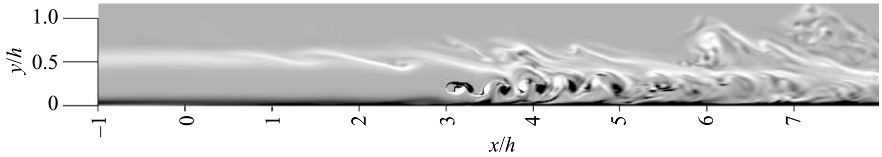

FIGURE 9. Spanwise vorticity $\omega/(V/h)$ field at $z/h=0.5$ and at $t/(h/V)=16.5$ for $Re=9000$, $D/h=0.1, l_c/h=3$ and $G/h=0.15$. The cylinder is located at $x/h=3$–3.1. Notice the presence of von Kármán vortex shedding for sufficiently large values of G/h.

recirculation regions along the bottom wall. Rather, they occur for the same reason as in constant-density flows, i.e. by the shedding of vortices closer to the cylinder in two-dimensional simulations (Mittal & Balachandar 1995).

During the transient stage ($t/(h/V)=3.3$–14), figure 8 shows that two-dimensional simulations significantly overpredict the amplitude of the force fluctuations, especially for the larger gap. This overprediction is caused by the more coherent Kelvin–Helmholtz billows in the two-dimensional simulations. We note from figures 8(a) and 8(c) that during the time interval $t=5$–10 there are about twice as many drag as lift cycles, in agreement with the typical behaviour of uniform Kármán vortex flow past an isolated cylinder. Figures 8(b) and 8(d) appear to suggest that two-dimensional simulations can capture the force fluctuations for the smaller G/h quite accurately, with the exception of the interval $t/(h/V)=4$–6. However, this good agreement is just coincidental: the value of l_c/h selected for the three-dimensional simulation is too small to allow for the breakup of the Kelvin–Helmholtz billows. When comparing the two-dimensional results with the three-dimensional reference case in figure 7, we notice a substantial discrepancy.

To summarize, two-dimensional simulations of gravity current flows past circular cylinders can be employed to obtain quantitative information for the impact stage. During the later stages, they correctly predict the dominant fluctuation frequency while overpredicting the fluctuation amplitude. This supports the two-dimensional results for gravity current flows with $H/h=5$ and $Re=2000$ and 6000 discussed in Gonzalez-Juez *et al.* (2009*b*). These conclusions are similar to those reached earlier for bottom-mounted square cylinders (Gonzalez-Juez *et al.* 2009*a*), even though they address a fundamentally different flow configuration with strong force fluctuations because of vortex shedding.

3.4. *Spanwise variation of the drag and associated flow structures*

3.4.1. *Impact stage*

Figure 10(a) shows a spanwise peak-to-peak variation of the drag of up to 30 % during impact. The following discussion provides evidence that this spanwise variation is governed by the gravity current's frontal lobe and cleft structure. Right after the gate at $x=0$ is opened (figure 1), a filamentary flow structure forms at the front of the current (Härtel, Carlsson & Thunblom 2000*a*; Härtel *et al.* 2000*b*) and later develops into the lobe and cleft structure (Simpson 1972) (cf. also figure 2*a*). The temporal evolution of this lobe and cleft structure before impact is visualized in figure 10(b) by means of the concentration $c^*=0.1$ isolines in the $y/h=0.002$ plane.

Figure 10 shows that the lobes hit the cylinder at approximately $z/h=0.16$, 0.42 and 0.77 and that the drag reaches instantaneous peaks at these locations during the impact stage. The other three-dimensional simulations conducted within this investigation display similar behaviour, as do earlier simulations for bottom-mounted

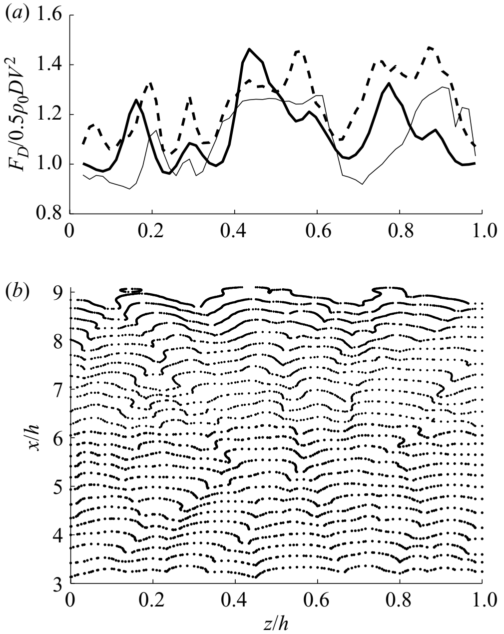

FIGURE 10. (*a*) Spanwise variation of the drag for $Re = 9000$, $D/h = 0.1$, $l_c/h = 9$ and $G/h = 0.03$ at different times during the impact stage: $t/(h/V) = 9.1$ (thick solid line), 9.2 (dashed line) and 9.3 (thin solid line). (*b*) Temporal evolution of the lobe and cleft structure before impact, visualized by the concentration $c^* = 0.1$ isolines in the $y/h = 0.002$ plane during the interval $3.5 < t/(h/V) < 9.2$. The cylinder is located at $x/h = 9$–9.1. The spanwise drag variation at impact is determined by the gravity current's lobe and cleft structure.

square cylinders (Gonzalez-Juez *et al.* 2009*a*). This suggests that the spanwise drag variation at impact is determined by the gravity current's lobe and cleft structure, even when a gap exists between the cylinder and the bottom wall. We remark that in the three-dimensional simulations with $l_c/h = 3$, even though the Kelvin–Helmholtz billows do not break up before the current meets the cylinder, a developed lobe and cleft structure is observed. An increase of the Reynolds number, from $Re = 9000$ in the reference case to $Re = 45\,000$, produces a somewhat smaller characteristic spanwise length scale of the drag variation (cf. figure 11), which results from smaller lobe sizes at higher values of Re (from data not shown here and from Simpson 1972). A spanwise drag variation governed by the lobe and cleft structure is also observed when the gap is increased, from $G/h = 0.03$ in the reference case to $G/h = 0.15$.

3.4.2. *Quasi-steady stage*

Figure 12 shows the spanwise variation of the drag at different times during the quasi-steady stage, as well as the drag value averaged during the interval $14.2 < t/(h/V) < 17.9$, for the simulations with $Re = 9000$, $l_c/h = 3$ and $G/h = 0.03$ and 0.15. The drag variation exhibits a characteristic length scale of the order of D, which is especially noticeable in the large-gap case. We remark that during the quasi-steady stage the lobe and cleft structure is not longer present.

For the larger-gap case ($G/h = 0.15$), figure 13 shows the presence of primary von Kármán vortices (cf. also figure 9) and of secondary streamwise vortices in the near wake. These flow structures are similar to those seen in the classic problem of constant-density flow past a circular cylinder at Re_D values of a few hundreds

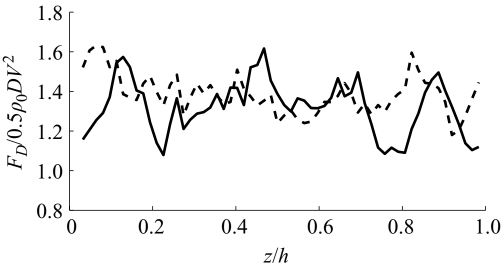

FIGURE 11. Spanwise variation of the drag for $Re = 45\,000$, $D/h = 0.1$, $l_c/h = 9$ and $G/h = 0.03$ at $t/(h/V) = 8.6$ (solid line) and 8.7 (dashed line) during impact.

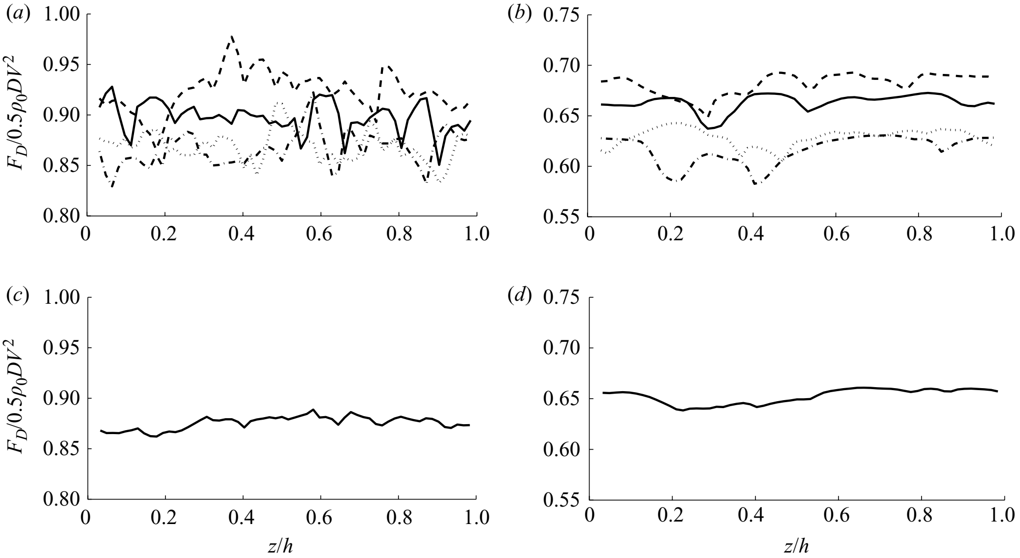

FIGURE 12. Spanwise variation of the drag for $Re = 9000$, $D/h = 0.1$, $l_c/h = 3$ and (*a*, *c*) $G/h = 0.15$ and (*b*, *d*) $G/h = 0.03$ at different times during the quasi-steady stage: $t/(h/V) = 14.2$ (solid lines), 15.3 (dashed lines), 16.5 (dashed-dotted lines) and 30 (dotted lines). The time-averaged drag is shown in (*c*) and (*d*). Notice the spanwise variation of the drag with a characteristic length of about a cylinder diameter D for the larger gap.

(Williamson 1996). We remark that $Re_D = UD/\nu = 459$ for the reference case, as discussed in § 3.5. The spacing of the streamwise vortices scales with D (cf. figure 13 for the gravity current flow and figure 14 in Williamson 1996 for the classic flow). Hence we can conclude that these vortices cause the D-scale spanwise drag variation in figure 12(*a*). Figures 13 and 14 show that a decrease of the gap considerably distorts the flow structures in the near wake, which explains the suppression of the D-scale spanwise drag variation in figure 12(*c*).

3.5. *Comparison with the classic flow past a circular cylinder*

For sufficiently large gaps, the above discussion indicates strong similarities between the quasi-steady wake flow structures and the classic constant-density flow past a circular cylinder. We will now quantify this level of agreement for $Re = 9000$, $l_c/h = 3$ and $G/h = 0.15$ by focusing on the mean drag, the peak-to-peak lift variation and the frequency of the force fluctuations (cf. the data in table 3).

Parameter	Gravity current flow	Classic flow
$F_{D,mean}/(0.5\rho_0 DU^2)$	1.25 (1 %)	1.24[†]
$F_{L,pp}/(0.5\rho_0 DU^2)$	1.11 (13 %)	1.28[†]
$f/(U/D)$	0.25 (19 %)	0.21[‡]

[†] Three-dimensional simulation by Mittal & Balachandar (1995).
[‡] Experiments by Prasad & Williamson (1997).

TABLE 3. Comparison of the mean drag $F_{D,mean}/(0.5\rho_0 DU^2)$, peak-to-peak lift $F_{L,pp}/(0.5\rho_0 DU^2)$ and frequency of the force fluctuations $f/(U/D)$ between the gravity current flow past a circular cylinder far away from the bottom wall at $Re_D = 459$ (three-dimensional simulation with $Re = 9000$, $l_c/h = 3$ and $G/h = 0.15$) and the classic constant-density flow past a circular cylinder in infinite domains at $Re_D = 525$ or $Re_D = 460$. The relative difference, indicated in per cent, is sufficiently small for constant-density flows to provide a useful approximation during the quasi-steady stage.

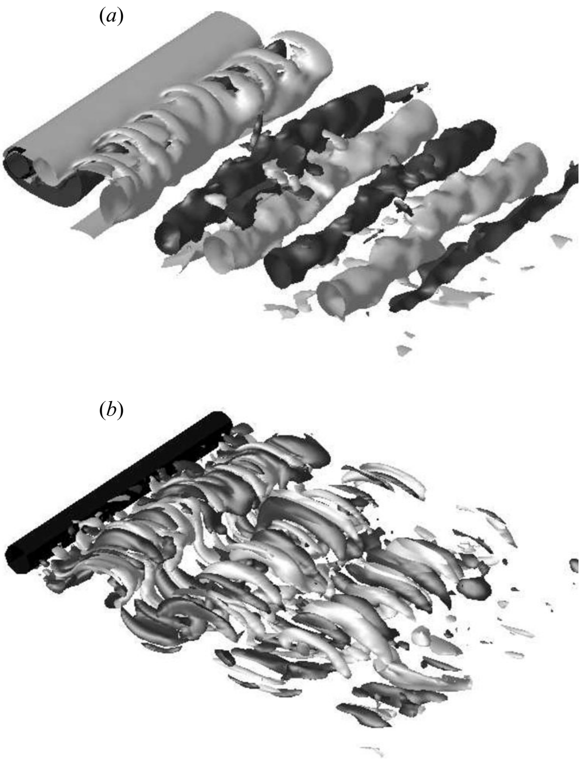

FIGURE 13. Instantaneous (*a*) spanwise and (*b*) streamwise vorticity isosurfaces ($\omega_z/(V/h) = 4$ and $\omega_x/(V/h) = 4$ in dark grey and $\omega_z/(V/h) = -4$ and $\omega_x/(V/h) = -4$ in light grey) during the quasi-steady stage for $Re = 9000$, $D/h = 0.1$, $l_c/h = 3$ and $G/h = 0.15$. Notice the presence of primary von Kármán vortices and of secondary streamwise vortices in the near wake.

For the gravity current flow, the effective free-stream velocity U is approximately constant during the quasi-steady stage, at a value $U = 0.86V$ (cf. figure 15). This agrees with the finding by Thomas, Dalziel & Marino (2003) that the fluid velocity within the gravity current some distance upstream of the head is lower than at the

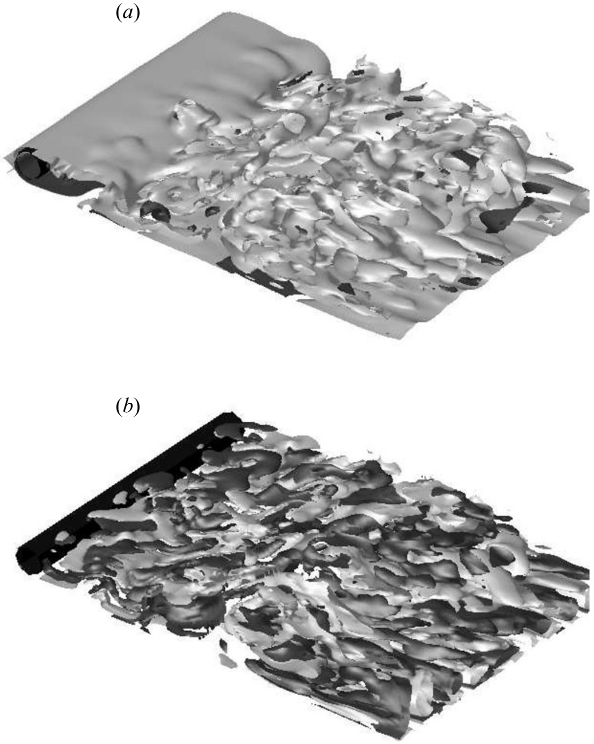

FIGURE 14. Instantaneous (*a*) spanwise and (*b*) streamwise vorticity isosurfaces ($\omega_z/(V/h)=4$ and $\omega_x/(V/h)=4$ in dark grey and $\omega_z/(V/h)=-4$ and $\omega_x/(V/h)=-4$ in light grey) during the quasi-steady stage for $Re=9000$, $D/h=0.1$, $l_c/h=3$ and $G/h=0.03$. A comparison with figure 13 indicates that reducing the gap size considerably distorts the flow structures in the near wake.

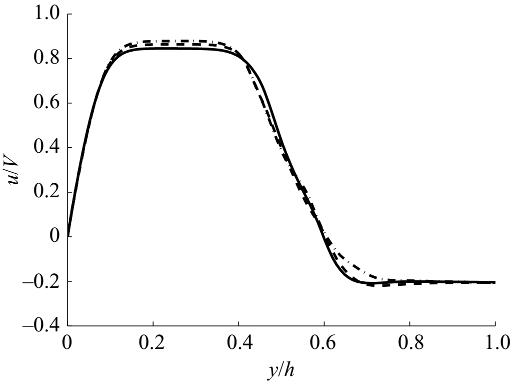

FIGURE 15. Time-averaged horizontal velocity profile upstream of the cylinder during the quasi-steady stage ($14.2 < t/(h/V) < 17.9$) for $Re=9000$, $D/h=0.1$, $l_c/h=3$ and $G/h=0.15$ at $z/h=0.5$ and $x/h=13.5$ (solid line), 14 (dashed line) and 14.5 (dash-dotted line). The cylinder is located at $y/h=0.15$–0.25.

head itself. The Reynolds number $Re_D=UD/\nu$ based on U and the cylinder diameter thus has a value of 459, which is sufficiently close to the values investigated by Mittal & Balachandar (1995) and Prasad & Williamson (1997) to make a valid comparison.

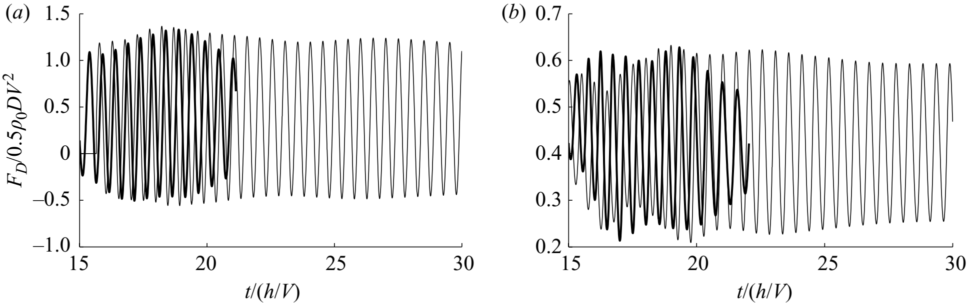

FIGURE 16. Comparison of lift fluctuations during the quasi-steady stage between 'long' (thin lines, $L/h=60$, $l/h=24$) and 'short' (thick lines, $L/h=24$, $l/h=12$) two-dimensional simulations for $Re=9000$, $D/h=0.1$, $l_c/h=3$ and (a) $G/h=0.15$ and (b) $G/h=0.03$. The amplitude and frequency of the lift fluctuations differ by less than 5 % when calculated from 34 shedding cycles instead of 8 cycles.

In this range of Reynolds numbers the quantities of interest depend only weakly on Re (Zdravkovich 1997; Norberg 2003).

The number of shedding cycles from which the quantities shown in table 3 are calculated can be increased by extending the computational domain L/h and the lock length l/h and by running the simulation for a longer time. Very long, two-dimensional simulations show that these quantities differ by less than 5 % when calculated from 34 shedding cycles ($L/h=60$, $l/h=24$) instead of 8 cycles ($L/h=24$, $l/h=12$). For example, we calculate from the lift fluctuations shown in figure 16(a) the difference of the peak-to-peak amplitude and frequency of the lift fluctuations of 5 % (2 %) and 3 % (1 %) respectively for $Re=9000$, $l_c/h=3$ and $G/h=0.15$ ($G/h=0.03$). Thus, we expect our calculation of the mean drag, peak-to-peak lift and frequency of the force fluctuations from eight shedding cycles of a three-dimensional simulation to be adequate for determining if there is a large difference in the values of the quantities shown in table 3 between the two types of flows considered here. The data shown in table 3 indicate that this difference is quite small. Hence the interaction between the mixing layer and the Kármán vortices, the mean lift component because of buoyancy and the slight wake deflection towards the bottom wall do not significantly influence the force loading for the present case. We conclude that in this parameter regime the force magnitude and frequency for quasi-steady gravity current flows over cylinders can be estimated, within some margin of error, on the basis of the available data from studies of constant-density flows past cylinders near walls (Bearman & Zdravkovich 1978; Zdravkovich 1985; Fredsøe & Hansen 1987; Chiew 1991; Lei *et al.* 1999, 2000).

4. Wall shear stress

In the following, we will analyse the dependence of the dimensionless friction velocity u_τ/V on the various flow parameters, because of its importance for the transport of sediment as discussed in § 1. The friction velocity is defined as

$$\frac{u_\tau}{V}=\sqrt{\frac{|\boldsymbol{\tau}_w|}{\rho_0 V^2}},\quad \frac{|\boldsymbol{\tau}_w|}{\rho_0 V^2}=\frac{1}{Re}\left(\frac{V}{u_b}\right)^{-1}\left[\sqrt{\left(\frac{\partial u/V}{\partial y/h}\right)^2+\left(\frac{\partial w/V}{\partial y/h}\right)^2}\right]_{y=0}. \tag{4.1}$$

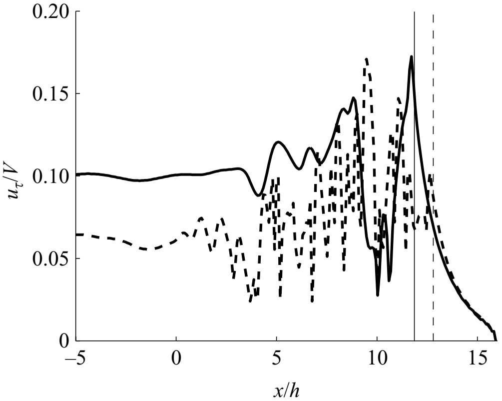

FIGURE 17. Streamwise variation of the friction velocity u_τ/V from two-dimensional simulations of gravity current flows without obstacles, for $H/h = 2.5$ and $Re = 2000$ (solid line) and $Re = 9000$ (dashed line). The front of the current is located at $x/h = 11.9$ ($x/h = 12.7$) for $Re = 2000$ ($Re = 9000$) and is indicated by a vertical solid (dashed) line. Note the larger friction velocities at the head of the current ($x/h \approx 12$), as compared with the tail ($-3 < x/h < 4$).

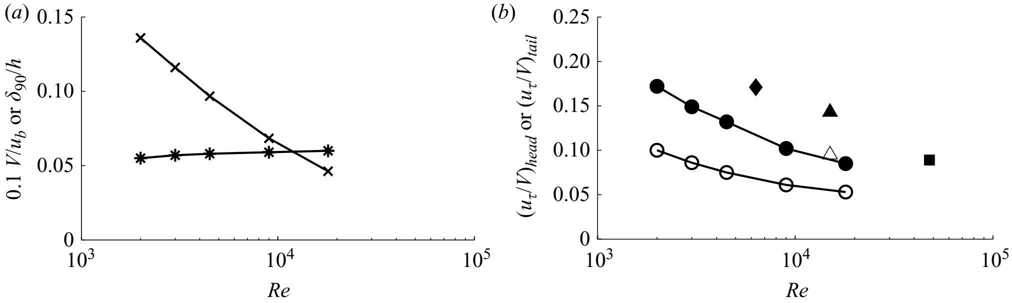

FIGURE 18. Effect of Re on the front speed (V/u_b, asterisks), boundary layer thickness (δ_{90}/h, crosses) and friction velocity at the head ($(u_\tau/V)_{head}$, filled circles) and at the tail ($(u_\tau/V)_{tail}$, open circles) from two-dimensional simulations of gravity currents without obstacles for $H/h = 2.5$. Also shown in (*b*) are the results for $(u_\tau/V)_{head}$ (filled symbols) and $(u_\tau/V)_{tail}$ (open symbols) from simulations of gravity currents with $H/h = 1$ and $l/h \sim 1$ by Ooi *et al.* (2009) (squares), Necker *et al.* (2002) (diamonds) and Cantero *et al.* (2008) (triangles).

4.1. *Gravity current flows without obstacles*

For reference purposes, we present data from two-dimensional simulations of gravity current flows without any obstacles. The parameters of these simulations are the same as in § 2.3 but with a grid of 1200 × 200 instead. Figure 17 shows the streamwise variation of the friction velocity for two values of Re at a time when the front of the current is near the end of the domain. Near the front, note the increase of the friction velocity in the upstream direction towards a maximum. This maximum is referred to as $(u_\tau/V)_{head}$. The friction velocity averaged over $-3 < x/h < 2$ is denoted as $(u_\tau/V)_{tail}$. We furthermore define the boundary layer thickness δ_{90}/h during the quasi-steady stage as the length over which the horizontal velocity averaged over $-3 < x/h < 2$ increases to 90 % of its maximum value.

Figure 18 shows that while V/u_b depends only weakly on Re, the other quantities decrease notably with Re. More importantly, figure 18(*b*) shows that the friction velocity at the head of the current is larger than that at the tail. We will employ this

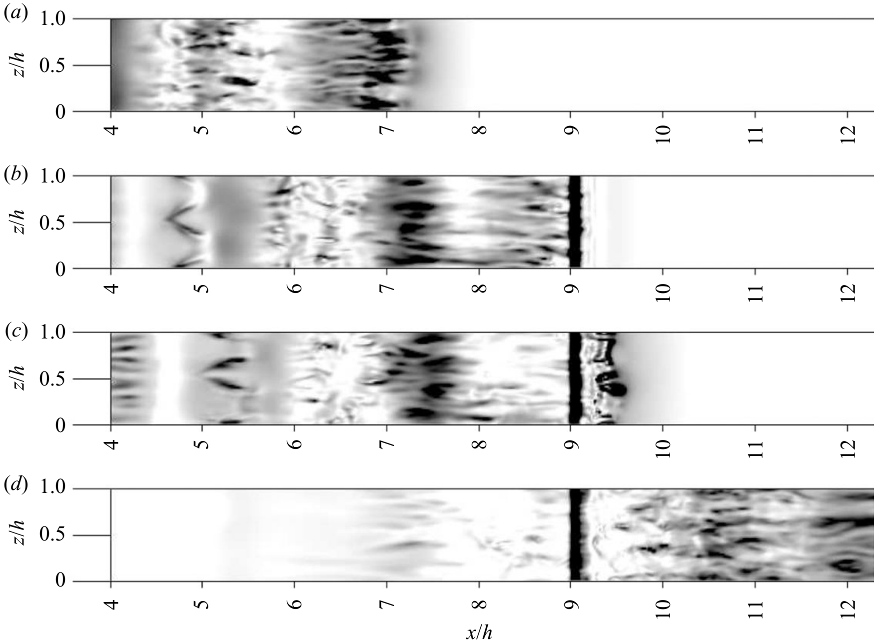

FIGURE 19. Friction velocity contours (u_τ/V) for $Re = 9000$, $D/h = 0.1$, $l_c/h = 9$ and $G/h = 0.03$ at different times: $t/(h/V) = (a)$ 7.3 (b) 9.4 (maximum friction velocity below the cylinder), (c) 9.9 and (d) 16.5. The cylinder is at $x/h = 9$–9.1. Darker shades indicate higher friction velocities.

information later in the analysis of gravity current flows past cylinders. Also note that the values for $(u_\tau/V)_{head}$ and $(u_\tau/V)_{tail}$ for $H/h = 2.5$ and $l/h = 12$ are close to those for $H/h = 1$ and $l/h \sim 1$ obtained in other studies (Necker *et al.* 2002; Cantero *et al.* 2008; Ooi *et al.* 2009).

4.2. *Reference case*

Figures 19 and 20 show the temporal evolution of friction velocity for the reference simulation ($Re = 9000$, $G/h = 0.03$ and $l_c/h = 9$), in which the cylinder is positioned at $x/h = 9$–9.1. The maximum friction velocity throughout the entire interaction occurs at $t/(h/V) = 9.3$, shortly after the time of maximum drag ($t/(h/V) = 9.2$), and at $x/h = 9.04$, just upstream of the cylinder's centre ($x/h = 9.05$). Large friction velocities are observed near the cylinder during the transient stage (cf. figure 21), especially as the head of the current plunges downward just downstream of the cylinder (cf. figures 3*d* and 20*c*). During the quasi-steady stage, the friction velocity right below the cylinder is approximately constant with time (figure 21) and about 30 % lower than at impact. The fluctuations of the friction velocity immediately downstream of the cylinder ($x/h = 9.1$–9.5) in figure 20(d) result from the shedding of vortices of negative vorticity (figure 3*f*), as will be discussed below. Similar observations hold for the case of $Re = 45\,000$.

Recall from figure 10(b) that the lobes first make contact with the cylinder at approximately $z/h = 0.16$, 0.42 and 0.77. Figure 22 shows that the friction velocity reaches local maxima at these spanwise positions, which indicates that the lobe and cleft structure governs the spanwise variation of the friction velocity at impact. Similar behaviour was observed in the other three-dimensional simulations.

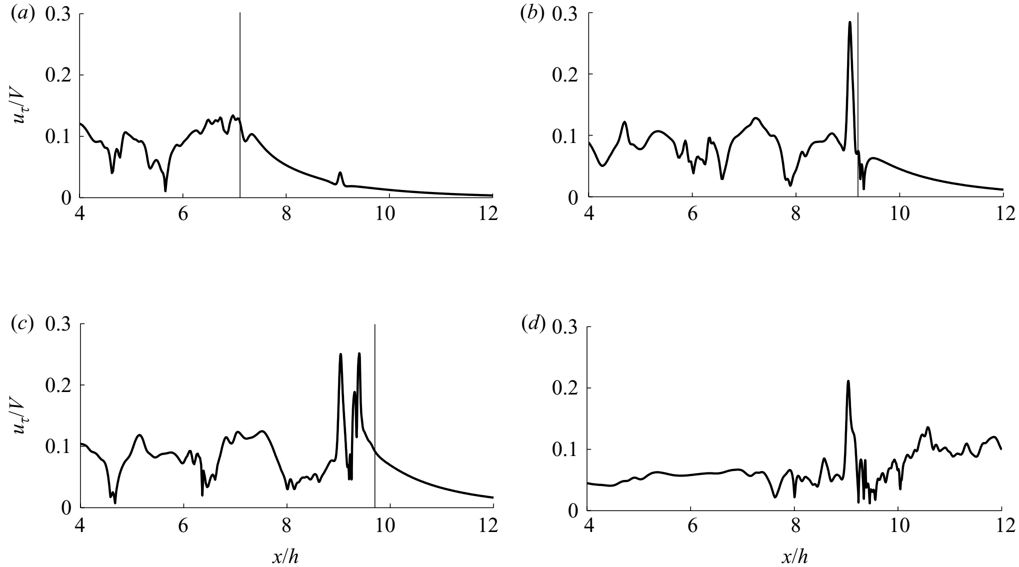

FIGURE 20. Streamwise variation of the friction velocity (u_τ/V) at $z/h = 0.5$ for $Re = 9000$, $D/h = 0.1$, $l_c/h = 9$ and $G/h = 0.03$ at different times: $t/(h/V) = $(*a*) 7.3, (*b*) 9.4 (maximum friction velocity below the cylinder), (*c*) 9.9 and (*d*) 16.5. The cylinder is located at $x/h = 9$–9.1. The front of the current using the $c^* = 0.5$ contour at $z/h = 0.5$ is indicated by the thin vertical lines. The maximum value of the friction velocity throughout the interaction occurs in (*b*). Also note the large friction velocities downstream of the cylinder in (*c*), as the current plunges downstream of the cylinder.

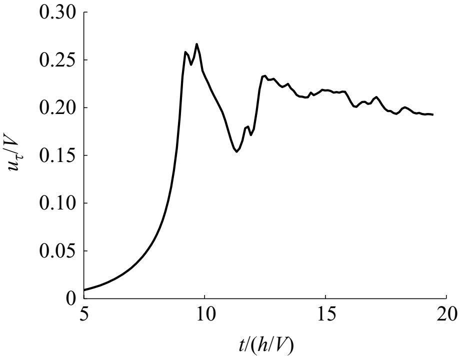

FIGURE 21. Temporal evolution of the spanwise-averaged friction velocity u_τ/V immediately below the centre of the cylinder ($x = l_c + D/2$), for $Re = 9000$, $D/h = 0.1$, $l_c/h = 9$ and $G/h = 0.03$.

4.3. *Range of validity of two-dimensional simulations*

Figures 23 and 24 show that during impact ($t/(h/V) < 3.2$) two-dimensional and three-dimensional simulation data for the spanwise-averaged maximum friction velocity agree to within 6 %. Of course, spanwise variations of the friction velocity are not captured by two-dimensional simulations. Figure 23 furthermore indicates that during the quasi-steady stage ($14.2 < t/(h/V) < 17.7$) the friction velocity tends towards a constant mean value, which is approximately identical in the two-dimensional and three-dimensional simulations. Similarly, figure 24 shows that two-dimensional and

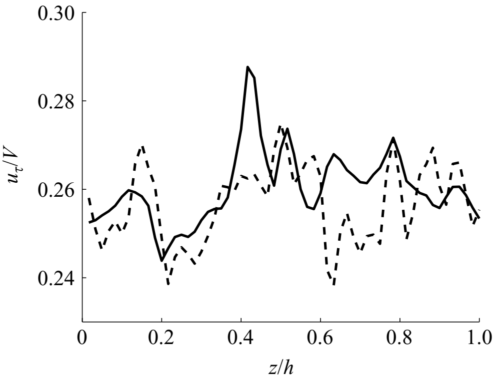

FIGURE 22. Spanwise variation of the friction velocity u_τ/V immediately below the cylinder centre at $x = l_c + D/2$, for $Re = 9000$, $D/h = 0.1$, $l_c/h = 9$ and $G/h = 0.03$ at $t/(h/V) = 9.2$ (solid line) and 9.3 (dashed line).

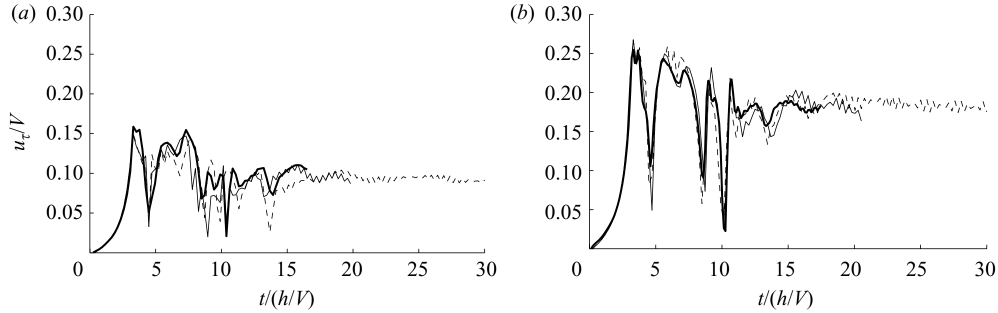

FIGURE 23. Comparison of the spanwise-averaged friction velocity u_τ/V immediately below the cylinder: two-dimensional (thin lines) and three-dimensional (thick lines) simulations for $Re = 9000$, $D/h = 0.1$, $l_c/h = 3$ and (*a*) $G/h = 0.15$ and (*b*) $G/h = 0.03$. The results from both 'long' (dashed thin lines, $L/h = 60$, $l/h = 24$) and 'short' (solid thin lines, $L/h = 24$, $l/h = 12$) two-dimensional simulations are shown.

three-dimensional simulations give comparable results for the streamwise variation of the friction velocity near the cylinder ($x/h = 2.9$–3.2).

For the transient stage ($3.2 < t/(h/V) < 14.2$), figure 23 displays large fluctuations of the friction velocity below the cylinder in both two-dimensional and three-dimensional simulations. Note, however, that this apparently good agreement is due to the short distance between the gate and the cylinder ($l_c/h = 3$), which does not allow for the complete breakup of the Kelvin–Helmholtz vortices in the three-dimensional simulations, as explained earlier. A comparison of figures 21 and 23(*b*) indicates significant differences when the two-dimensional simulation is compared with the three-dimensional simulation for $l_c/h = 9$, in which the Kelvin–Helmholtz vortices break up before encountering the cylinder. To conclude, two-dimensional simulations provide accurate information for the friction velocity immediately below the cylinder during the impact stage and for the time-averaged values during the quasi-steady stage.

4.4. *Effect of the gap*

Figure 25 displays the effect of the gap size G/h on the streamwise variation of the friction velocity near the cylinder (*a*) at impact and (*b*) during the quasi-steady stage.

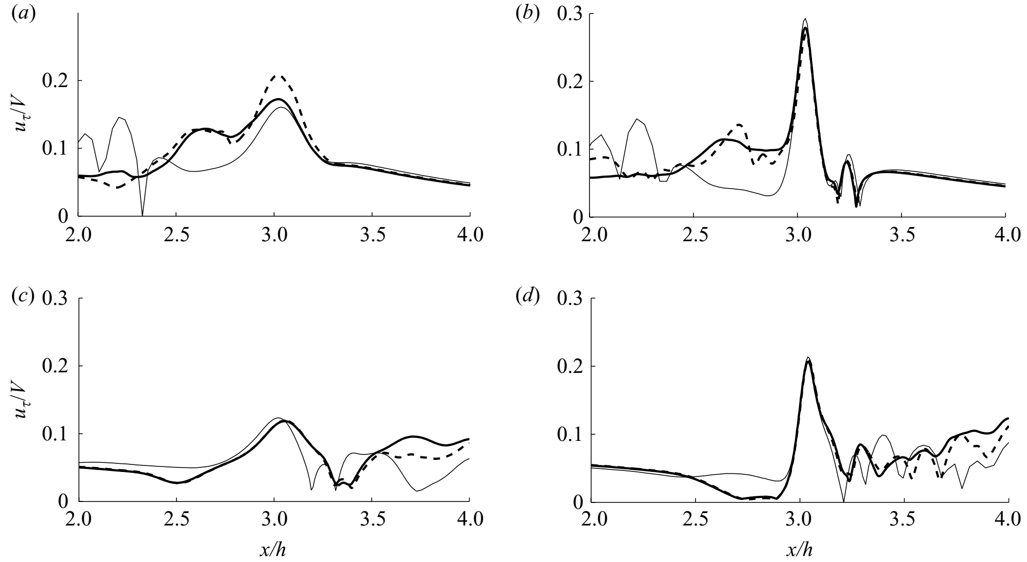

FIGURE 24. Comparison of the streamwise variation of the friction velocity u_τ/V near the cylinder: two-dimensional (thin lines) and three-dimensional (thick lines) simulations for $Re=9000$, $D/h=0.1$, $l_c/h=3$ and (*a*, *c*) $G/h=0.15$ and (*b*, *d*) $G/h=0.03$. Times are (*a*, *b*) $t/(h/V)=3.3$ and (*c*, *d*) $t/(h/V)=15.3$. In (*a*) and (*b*) the current front is located at $x/h\approx 3.2$, while in (*c*) and (*d*) it has reached $x/h\approx 14.4$. Both the spanwise-averaged (solid lines) and the $z/h=0.5$ (dashed lines) values of u_τ/V are shown from the three-dimensional simulations. The cylinder is located at $x/h=3$–3.1.

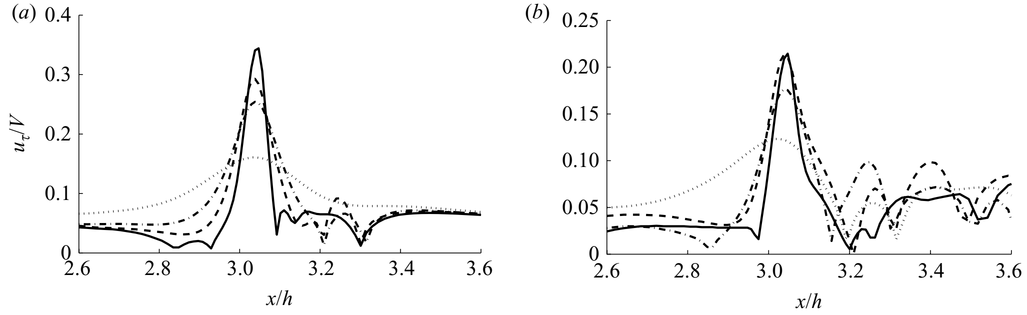

FIGURE 25. Effect of G/h on the streamwise variation of the friction velocity u_τ/V near the cylinder at impact (*a*, $t/(h/V)=3.3$) and during the quasi-steady stage (*b*, $t/(h/V)=15.3$). Two-dimensional simulations for $Re=9000$, $D/h=0.1$, $l_c/h=3$ and different values of G/h: 0.015 (solid line), 0.03 (dashed line), 0.05 (dash-dotted line) and 0.15 (dotted line). The cylinder is located at $x/h=3$–3.1. The maximum friction velocity occurs below the cylinder and decreases for larger gaps.

The maximum friction velocity occurs below the cylinder and decreases for larger gaps.

When vortex shedding is present during the quasi-steady stage, it results in friction velocity fluctuations downstream of the cylinder (cf. figure 25*b*). While the peak of these fluctuations is largest for intermediate gap sizes, we have to keep in mind that two-dimensional simulations generally overpredict the fluctuation amplitudes (cf. figure 24*d*).

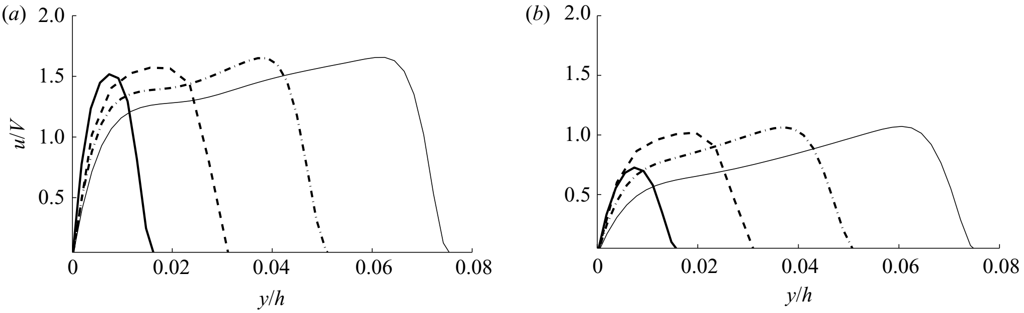

FIGURE 26. Effect of G/h on the horizontal velocity profile within the gap (*a*) at impact ($t/(h/V) = 3.3$) and (*b*) during the quasi-steady stage ($t/(h/V) = 15.3$). Two-dimensional simulations for $Re = 9000$, $D/h = 0.1$, $l_c/h = 3$ and different values of G/h: 0.015 (thick solid line), 0.03 (dashed line), 0.05 (dashed-dotted line) and 0.075 (thin solid line).

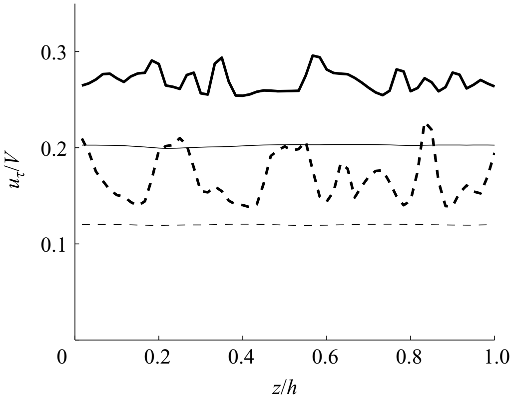

FIGURE 27. Effect of G/h on the spanwise variation of the friction velocity u_τ/V below the cylinder at impact (thick lines, $t/(h/V) = 3.3$) and during the quasi-steady stage (thin lines, $t/(h/V) = 15.3$). The data are from three-dimensional simulations for $Re = 9000$, $D/h = 0.1$, $l_c/h = 3$ and different values of G/h: 0.03 (solid lines) and 0.15 (dashed lines). While the mean friction velocity is lower for larger gaps, its spanwise variation is more pronounced.

Figure 26 shows the influence of the gap size G/h on the horizontal velocity profile inside the gap, at $x = l_c + D/2$, (*a*) during impact and (*b*) during the quasi-steady stage. We note that the maximum horizontal velocity in the gap remains approximately constant in the range $G/h = 0.03$–0.075 ($G/D = 0.3$–0.75). This finding is consistent with the open-channel flow experiments of Fredsøe & Hansen (1987) and Chiew (1991), who observed a small effect of G/D on the average and maximum velocities in the gap for $G/D \geqslant 0.12$.

Since the maximum horizontal velocity in the gap is approximately constant over the range $G/h = 0.03$–0.075, it cannot explain the increasing friction velocity for smaller gaps. However, we note in figure 26(*a*) change in the shape of the velocity profile when the gap is increased from $G/h = 0.015$, which suggests a potential transition between different flow regimes. This issue will be further analysed for a larger set of parameters in § 5.

Figure 27 shows the spanwise peak-to-peak variation of the friction velocity during impact. Values up to $0.04V$ (15 %) and $0.09V$ (50 %) are reached for $G/h = 0.03$ and $G/h = 0.15$, respectively. Interestingly, while the friction velocity is lower for larger gaps, its spanwise variation is more pronounced. As discussed earlier for the reference

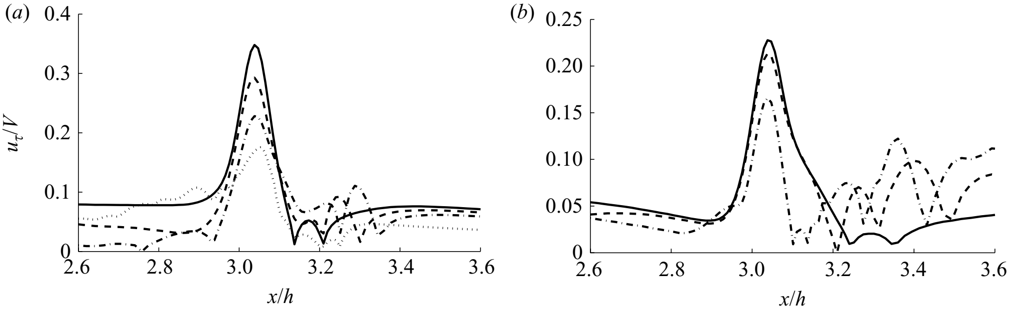

FIGURE 28. Effect of Re on the streamwise variation of the friction velocity u_τ/V near the cylinder (a) at impact ($t/(h/V)=3.3$) and (b) during the quasi-steady stage ($t/(h/V)=15.3$). Data are from two-dimensional simulations for $D/h=0.1$, $G/h=0.03$, $l_c/h=3$ and different values of Re: 4500 (solid line), 9000 (dashed line) and 18 000 (dash-dotted line). The dotted line in (a) shows the friction velocity at $z/h=0.5$ from the three-dimensional simulation with $Re=45\,000$. The cylinder is located at $x/h=3$–3.1.

case, the spanwise variation of the friction velocity at impact is governed by the lobe and cleft structure. During the quasi-steady stage, the spanwise variations are minimal.

4.5. *Effect of the Reynolds number*

For $G/h=0.03$, figure 28 shows that the maximum friction velocity below the cylinder decreases with increasing Re. This is expected, since from definition (4.1) $u_\tau/V \rightarrow 0$ as $Re \rightarrow \infty$. In addition, we found (not shown) that as we increase Re from 2000 to 18 000 for $G/h=0.03$, the horizontal velocities in the gap increase, while the pressure gradient below the cylinder remains approximately constant. The implications of this for u_τ/V will be further discussed in § 5 for a larger set of parameters. The Reynolds number Re has a similar influence on the spanwise variations of drag and friction velocity at impact: the characteristic length scale of these variations decreases as Re increases, because of smaller lobes.

4.6. *Dominant parameters*

We will now attempt to quantify the dependence of the friction velocity below the cylinder on the dominant parameters of the problem. Towards this end, we take as the representative friction velocity during the impact stage the maximum value in the intervals $2.95 < x/h < 3.15$ and $2.8 < t/(h/V) < 3.8$. As representative quasi-steady friction velocity, we take the time-averaged value at $x/h=3.05$.

This time-averaged value is calculated over a time interval of approximately four dimensional time units (h/V), during which 8–10 shedding cycles occur whenever vortex shedding is present. Such time interval is selected so that the convection of vortical structures along the bottom wall towards the cylinder and that of Kelvin–Helmholtz vortices at the fluids interface has ceased. As discussed previously in § 3.5, the quasi-steady friction velocity calculated from 30–35 cycles of ‘long’ two-dimensional simulations is within that calculated from 8–10 cycles of ‘short’ simulations. For example, we calculate from figure 23(a) difference between the quasi-steady friction velocity of ‘long’ ($L/h=60$, $l/h=24$) and ‘short’ ($L/h=24$, $l/h=12$) two-dimensional simulations of 7 % (3 %) for $Re=9000$, $l_c/h=3$ and $G/h=0.15$ ($G/h=0.03$).

The friction velocity u_τ below the cylinder depends on

$$u_\tau = f\,(G, D, \delta_{90}, V, \nu)\,. \tag{4.2}$$

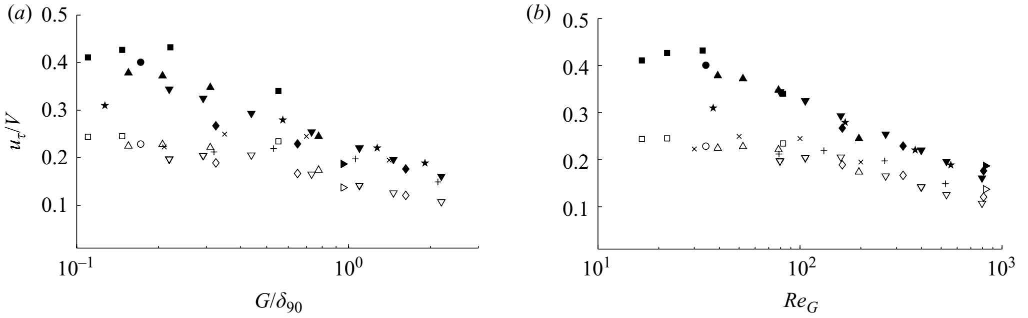

FIGURE 29. Effect of (*a*) G/δ_{90} and (*b*) Re_G on the maximum (closed symbols) and quasi-steady (open symbols) friction velocity u_τ/V for $H/h=2.5$, $D/h=0.1$, $l_c/h=3$ and different values of G/h and Re. The different values of Re are denoted as follows: $Re=2000$ (squares), 3000 (circles), 4500 (triangles), 9000 (inverted triangles), 18 000 (diamonds) and 45 000 (right triangle). The results from simulations for larger cylinders with $D/h=0.15$, $H/h=5$ and $Re=6000$ are also shown (stars). Data from two-dimensional simulations of constant-density boundary layer flows past a circular cylinder near a bottom wall at $Re_D=200$ (crosses) and $Re_D=525$ (plus signs) are indicated for comparison.

The lock height h is not included among the list of parameters, since in practice gravity current heights of $h/2$ (Simpson 1997; Shin *et al.* 2004) are much larger than D and G, as discussed in §2.3. We note that if V were not included, then h would enter the dependency through $\sqrt{g'h}$. By taking G and V as the repeating variables in the above dependency, Buckingham's Π-theorem gives

$$\frac{u_\tau}{V}=F\left(\frac{G}{D},\frac{G}{\delta_{90}},Re_G\right), \tag{4.3}$$

where Re_G is a gap Reynolds number defined as $Re_G=VG/\nu$. However, the parameters we control directly in the simulations are G/h, Re and D/h, so that we can modify the values of the parameters in the above relation only indirectly; G/D is varied by changing G/h in the range $G/h=0.015$–0.15 and by employing both $D/h=0.1$ and $D/h=0.15$; G/δ_{90} is varied through G/h and Re; Re is related to δ_{90}/h as shown in figure 18(*a*). Here Re is changed in the range $Re=2000$–$45\,000$. Finally, the gap Reynolds number Re_G is varied by changing G/h and Re, since $Re_G=Re(G/h)(V/u_b)$.

While we observed an overall decrease of the maximum and quasi-steady friction velocities for increasing G/D, there was substantial scatter in the data when we graphed them against G/D. On the other hand, we obtained better collapse when plotting the data against G/δ_{90} and Re_G. The dependence of the maximum and quasi-steady friction velocities on these parameters is shown in figure 29. Note the particularly good collapse of the data as function of Re_G.

5. Implications for scour

To isolate the effect of the cylinder presence on the friction velocity it is useful to analyse the ratio of the friction velocities with and without the cylinder. This ratio is commonly referred to as the amplification factor AF in scour studies (Sumer & Fredsøe 2002). We define the impact amplification factor as the ratio of the maximum friction velocity immediately below the cylinder to the friction velocity at the head of

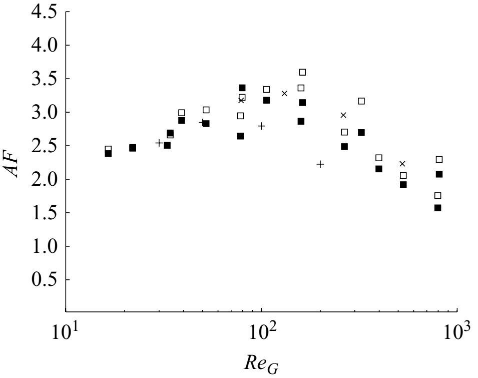

FIGURE 30. Effect of Re_G on the impact (filled squares) and quasi-steady (open squares) values of the amplification factor (AF) for $H/h=2.5$, $D/h=0.1$, $l_c/h=3$ and different values of G/h and Re. Also shown are the results from two-dimensional simulations of constant-density boundary layer flows past a circular cylinder near a bottom wall at $Re_D=200$ (crosses) and $Re_D=525$ (plus signs). The impact amplification factor is comparable to the quasi-steady value.

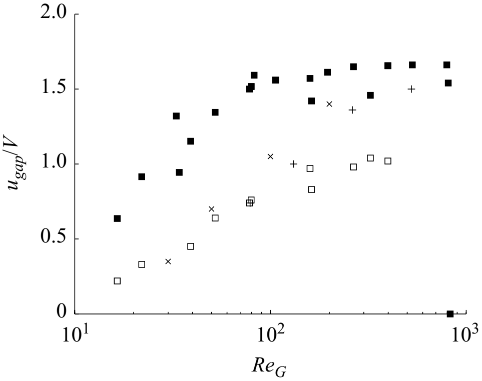

FIGURE 31. Effect of Re_G on the maximum velocity in the gap during the impact (filled squares, $t/(h/V)=3.3$) and quasi-steady (open squares) stages. Simulation parameters are $H/h=2.5$, $D/h=0.1, l_c/h=3$ and different values of G/h and Re. Data from two-dimensional simulations of constant-density boundary layer flows past a circular cylinder near a bottom wall at $Re_D=200$ (crosses) and $Re_D=525$ (plus signs) are indicated for comparison.

a current without cylinder (cf. §4.1). A corresponding definition is employed for the quasi-steady amplification factor.

Figure 30 shows that AF increases with Re_G for $Re_G \lesssim O(100)$, while it decreases for higher Re_G. For $Re_G \lesssim O(100)$, more of the faster-moving fluid away from the wall enters inside the gap as Re_G increases (cf. figure 31), so that AF increases. In figure 31, u_{gap}/V is the maximum horizontal velocity at $x/h=3.05$, and its value at $t/(h/V)=3.3$ is employed to characterize the impact stage, while a temporally averaged value is used for the quasi-steady stage. On the other hand, notice in figure 31 that the velocities inside the gap stay approximately constant for $Re_G \gtrsim O(100)$. When $Re_G \gtrsim O(100)$, AF decreases as Re_G increases. This is expected, since at very large values of Re_G the amplification factor would reach the asymptote $AF=1$, at which

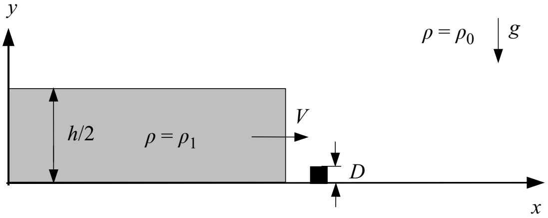

FIGURE 32. Gravity current of height $h/2$ about to encounter a bottom-mounted square cylinder of side D.

the cylinder is ‘far enough’ from the bottom wall so that its presence is ‘not felt’ at the bottom wall.

Figure 30 also shows that the amplification factor during impact is about the same as during the quasi-steady stage. In other words, the presence of the cylinder amplifies proportionally the friction velocity of a current without obstacle during all stages of the interaction.

We can now compare the above results with those from two-dimensional simulations of constant-density boundary layer flows past circular cylinders near walls at $Re_D = UD/\nu$ of 200 and 525, where U is the horizontal velocity outside the boundary layer. The gap G/D is varied in the range $G/D = 0.15$–1.5. The complete parameters of these two-dimensional simulations can be found in Gonzalez-Juez (2009). We find that for gravity currents and constant-density flows, Re_G has a similar effect on the friction velocity below the cylinder (figure 29*b*), on the amplification factor (figure 30) and on the maximum horizontal velocity in the gap (figure 31). (Note that V denotes the front velocity for the gravity current and the free-stream velocity for the constant-density flow.) Hence, if we know the friction velocities at the head and tail of a gravity current without obstacle (§ 4.1), we can employ the amplification factor for constant-density flows past cylinders near walls to estimate the friction velocity for gravity currents in the presence of a cylinder.

We now discuss the onset of scour near a pipe embedded in an erodible bed of uniform and cohesionless sediment. Scour starts when the difference in pressure upstream and downstream of the pipe Δp, which induces a seepage flow beneath the pipe, is sufficiently large to break the soil under the pipe, a process that is referred to as piping. A necessary condition for this break to occur is (Chiew 1990; Sumer *et al.* 2001)

$$\frac{\Delta p/(\rho_0 g)}{\Delta x} \geqslant i_f. \tag{5.1}$$

Here Δx is the streamwise distance across which the pressure difference is established, and i_f denotes a property of the bed called the floatation gradient. The pressure gradient $\Delta p/(\rho_0 g \Delta x)$ can be either dynamic or static (Chiew 1990; Sumer *et al.* 2001). A further necessary condition is that $\Delta p/(\rho_0 g \Delta x)$ must be maintained for a sufficiently long time, or, if cyclic and with a short time period, $\Delta p/(\rho_0 g \Delta x)$ should occur repeatedly (Sumer *et al.* 2001). Past studies have addressed the onset of scour in both steady and wavy flows (e.g. Mao 1986; Chiew 1990; Sumer *et al.* 2001).

The pressure difference $\Delta p/(\rho_0 g \Delta x)$ for bottom-mounted square cylinders in gravity current flows can now be estimated, along with the time interval over which this pressure difference is maintained. Towards this end, we will make partial use of the results obtained by Gonzalez-Juez *et al.* (2009*a*). Consider a gravity current of height $h/2$ about to encounter a bottom-mounted square cylinder of side D (cf. figure 32), under the realistic conditions of $h \ll H$ and $D \ll h$. The hydrostatic pressure at $y = 0$ (the sediment bed surface) immediately upstream of the cylinder can be estimated as $\rho_0 g(H - h/2) + \rho_1 g h/2$, while its counterpart immediately downstream of the cylinder is $\rho_0 g H$. The dynamic pressure is estimated as $0.5\rho_0 V^2$ upstream of the cylinder and as zero downstream, since the wake is very weak at impact (Gonzalez-Juez *et al.* 2009*a*). For an inviscid gravity current with $h \ll H$, Shin *et al.* (2004) predicted a front speed of $V = \sqrt{g'h/2}$. Thus, by taking $\Delta x = D$, we obtain

$$\frac{\Delta p/(\rho_0 g)}{\Delta x} = 0.75 \left(\frac{D}{h}\right)^{-1} \left(\frac{\Delta\rho}{\rho_0}\right). \tag{5.2}$$

Because the flow is essentially inviscid ($Re \to \infty$), (5.2) is applicable to full-scale flows. By combining (5.1) and (5.2), we obtain the following preliminary criterion for the onset of scour when a gravity current encounters a submerged cylinder:

$$0.75 \left(\frac{D}{h}\right)^{-1} \left(\frac{\Delta\rho}{\rho_0}\right) \geqslant i_f. \tag{5.3}$$

Typical submarine applications may involve parameter values $D/h \approx 0.005$–0.5 (cf. § 2.3) and $\Delta\rho/\rho_0 \lesssim 0.05$. We can assume $i_f \approx 1$, on the basis of the values of 0.9 and 0.77 determined experimentally by Chiew (1990) and Sumer *et al.* (2001), respectively. We conclude that it is possible for inequality (5.3) to be satisfied by typical Boussinesq gravity currents, so that piping may occur.

It remains to be shown that the pressure difference given by (5.2) can be sustained for sufficiently long times. Towards this end, we assume that the time interval during which this pressure difference is sustained, Δt, scales with the time D/V it takes for the gravity current to advance one cylinder diameter. With $V = \sqrt{g'h/2}$ we obtain $D/V = \sqrt{2D^2/(g'h)}$. Typical gravity current heights $h/2$ are 10–100 m in the ocean (Kneller *et al.* 1999) and 0.05–0.5 m in the laboratory. We take a characteristic cylinder diameter of 1 m for ocean conditions and 0.01 m for laboratory conditions and a density difference of $\Delta\rho/\rho_0 \approx 0.01$. Thus, we obtain $\Delta t \sim 1$ *s* for ocean conditions and $\Delta t \sim 0.1$ *s* for laboratory conditions. Since Sumer *et al.* (2001) have reported that a time interval of 5 s suffices for piping to occur under the conditions of their experiments, while 0.5 s does not, our estimates for the time interval over which $\Delta p/(\rho_0 g)/\Delta x$ is maintained suggest that piping may occur in the ocean, while it will probably not occur in the laboratory.

We conclude that a sufficiently large pressure difference may be maintained over a long enough time interval for piping to occur in the ocean. We also note that the lobe and cleft structure may well cause substantial spanwise variations of this pressure difference (cf. § 3.4), so that scouring may be initiated locally (Sumer & Fredsøe 2002).

6. Summary and conclusions

The present investigation has focused on the flow of compositional gravity currents past circular cylinders mounted above a non-erodible wall. It employs Navier–Stokes simulations to quantify the force load on the cylinder, along with the friction velocity at the bottom wall near the cylinder. The simulation results are then analysed with a view towards the occurrence of scour near pipelines mounted on erodible beds. In order to address practically relevant situations, we consider a sufficiently large ratio of the channel height and the lock height ($H/h = 2.5$) and a small ratio of the cylinder diameter and the lock height ($D/h = 0.1$). The Reynolds numbers in the range of 2000–45 000 are typical for laboratory-scale flows.

Comparisons of two-dimensional and three-dimensional simulations show that two-dimensional simulations accurately capture the overall features of the impact stage. Clearly, three-dimensional simulations are required to reproduce the spanwise variations caused by the lobe and cleft structure. Throughout the transient stage, two-dimensional simulations notably overpredict the fluctuations of the force load and friction velocity, because of unphysically coherent Kelvin–Helmholtz billows. During the quasi-steady stage, two-dimensional simulations give accurate results for the spanwise and temporally averaged friction velocity below the cylinder, as long as there are no separated flow regions propagating along the bottom wall. These findings support previous results from two-dimensional simulations by Gonzalez-Juez *et al.* (2009*b*).

Comparisons between gravity current and constant-density flows past circular cylinders show that the impact and transient stages are unique to gravity current flows. On the other hand, there are strong similarities between the two during the quasi-steady stage: specifically, the wake structures are similar, and the values of the drag, peak-to-peak lift, vortex shedding frequency and friction velocity below the cylinder are comparable. Consequently, the values of these quantities during the quasi-steady stage of a gravity current flow can be estimated to within 10–20 % (for the parameters considered here) using existing data for the well-studied constant-density flow past a circular cylinder near a wall.

The mechanisms governing the dynamics of the flow in the gap are discussed, and it is shown that the friction velocity below the cylinder depends chiefly on the Reynolds number Re_G formed with the front velocity and the gap width. The maximum friction velocity at impact is about 1.6 times larger than during the quasi-steady stage or in constant-density flows. Hence aggressive tunnelling erosion can occur at impact, which represents a key difference between the scour dynamics of gravity current and constant-density flows. Furthermore, the larger friction velocity near the lobes (by about 15 %) may trigger localized scour. During the quasi-steady stage, as a result of vortex shedding for sufficiently large gaps, lee-wake erosion may occur. We note that the above-given comments are based on the friction velocity data obtained from simulations for non-erodible beds. Clearly, future research should extend the scope of the simulations to erodible boundaries, non-Boussinesq currents (Birman, Martin & Meiburg 2005; Lowe, Rottman & Linden 2005), sloping terrains (Birman *et al.* 2007*a*), stratified ambient and the effects of internal waves (Maxworthy *et al.* 2002; Birman, Meiburg & Ungarish 2007*b*; Munroe *et al.* 2009), and it should involve comparisons with corresponding laboratory experiments.

The authors wish to acknowledge several helpful discussions with Prof. Stephen McLean. E.G.-J. is being supported by the National Science Foundation IGERT grant DGE02-21715, as well as by a Cota-Robles fellowship. Computing time has been provided by the California NanoSystems Institute at UC Santa Barbara and Hewlett-Packard and by the National Center for High Performance Computing in Taiwan.

REFERENCES

Bearman, P. W. & Zdravkovich, M. M. 1978 Flow around a circular cylinder near a plane boundary. *J. Fluid Mech.* **89**, 33–47.

Benjamin, T. B. 1968 Gravity currents and related phenomena. *J. Fluid Mech.* **31**, 209–248.

Birman, V. K., Battandier, B. A., Meiburg, E. & Linden, P. F. 2007*a* Lock-exchange flows in sloping channels. *J. Fluid Mech.* **577**, 53–77.

Birman, V. K., Martin, J. E. & Meiburg, E. 2005 The non-Boussinesq lock-exchange problem. Part 2. High-resolution simulations. *J. Fluid Mech.* **537**, 125–144.

Birman, V. K., Meiburg, E. & Ungarish, M. 2007*b* On gravity currents in stratified ambients. *Phys. Fluids* **19**, 086602.

Blanchette, F., Strauss, M., Meiburg, E., Kneller, B. & Glinsky, M. E. 2005 High-resolution numerical simulations of resuspending gravity currents: conditions for self-sustainment. *J. Geophys. Res.* **110**, C12022.

Bruschi, R., Bughi, S., Spinazze, M., Torselletti, E. & Vitali, L. 2006 Impact of debris flows and turbidity currents on seafloor structures. *Norw. J. Geol.* **86**, 317–337.

Cantero, M. I., Balachandar, S., Garcia, M. H. & Bock, D. 2008 Turbulent structures in planar gravity currents and their influence on the flow dynamics. *J. Geophys. Res.* **113**.

Cantero, M. I., Lee, J. R., Balachandar, S. & Garcia, M. H. 2007 On the front velocity of gravity currents. *J. Fluid Mech.* **586**, 1–39.

Chang, K. S., Constantinescu, G. & Park, S.-O. 2006 Analysis of the flow and mass transfer processes for the incompressible flow past an open cavity with a laminar and a fully turbulent incoming boundary layer. *J. Fluid Mech.* **561**, 113–145.

Chang, K. S., Constantinescu, G. & Park, S.-O. 2007*a* The purging of a neutrally buoyant or a dense miscible contaminant from a rectangular cavity. Part I. The case of an incoming laminar boundary layer. *J. Hydraul. Engng* **133**, 361–372.

Chang, K. S., Constantinescu, G. & Park, S.-O. 2007*b* The purging of a neutrally buoyant or a dense miscible contaminant from a rectangular cavity. Part II. The case of an incoming fully turbulent overflow. *J. Hydraul. Engng* **133**, 373–385.

Chiew, Y. 1991 Flow around horizontal circular cylinder in shallow flows. *J. Waterway Port Coast. Ocean Engng* **117** (2), 120–135.

Chiew, Y. M. 1990 Mechanics of local scour around submarine pipelines. *J. Hydraul. Engng* **116** (4), 515–529.

Dengler, A. T. & Wilde, P. 1987 Turbidity currents on steep slopes: application of an avalanche-type numeric model for ocean thermal energy conversion design. *Ocean Engng* **14**, 409–433.

Ermanyuk, E. V. & Gavrilov, N. V. 2005*a* Interaction of an internal gravity current with a submerged circular cylinder. *J. Appl. Mech. Tech. Phys.* **46** (2), 216–223.

Ermanyuk, E. V. & Gavrilov, N. V. 2005*b* Interaction of an internal gravity current with an obstacle on the channel bottom. *J. Appl. Mech. Tech. Phys.* **46** (4), 489–495.

Fredsøe, J. & Hansen, E. A. 1987 Lift forces on pipelines in steady flow. *J. Waterway Port Coast. Ocean Engng* **113** (2), 139–155.

Germano, M., Piomelli, U., Moin, P. & Cabot, W. H. 1991 A dynamic subgrid-scale eddy viscosity model. *Phys. Fluids* **3** (7), 1760–1765.

Gonzalez-Juez, E. D. 2009 Gravity current – submarine structure interaction: hazard analysis via high-resolution simulations. PhD thesis, University of California at Santa Barbara, Santa Barbara, CA.

Gonzalez-Juez, E. D., Constantinescu, S. G. & Meiburg, E. 2007 A study of the interaction of a gravity current with a square cylinder using two-dimensional numerical simulations. In *Proceedings of the 26th International Conference on Offshore Mechanics and Arctic Engineering*, San Diego, CA.

Gonzalez-Juez, E. D. & Meiburg, E. 2009 Shallow water analysis of gravity current flows past isolated obstacles. *J. Fluid Mech.* **635**, 415–438.

Gonzalez-Juez, E. D., Meiburg, E. & Constantinescu, S. G. 2009*a* Gravity currents impinging on submerged cylinders: flow fields and associated forces. *J. Fluid Mech.* **631**, 65–102.

Gonzalez-Juez, E. D., Meiburg, E. & Constantinescu, S. G. 2009*b* The interaction of a gravity current with a circular cylinder mounted above a wall: effect of the gap size. *J. Fluid Struct.* **25**, 629–640.

Graf, W. H. 1984 *Hydraulics of Sediment Transport*. Water Resources.

Härtel, C., Carlsson, F. & Thunblom, M. 2000*a* Analysis and direct numerical simulation of the flow at a gravity-current head. Part 2. The lobe-and-cleft instability. *J. Fluid Mech.* **418**, 213–229.

Härtel, C., Meiburg, E. & Necker, F. 2000*b* Analysis and direct numerical simulation of the flow at a gravity-current head. Part 1. Flow topology and front speed for slip and no-slip boundaries. *J. Fluid Mech.* **418**, 189–212.

Kneller, B., Bennett, S. J. & McCaffrey, W. D. 1999 Velocity structure, turbulence and fluid stresses in experimental gravity currents. *J. Geophys. Res.* **104** (C3), 5381–5391.

Lei, C., Cheng, L., Armfield, S. W. & Kavanagh, K. 2000 Vortex shedding suppression for flow over a circular cylinder near a plane boundary. *Ocean Engng* **27** (10), 1109–1127.

Lei, C., Cheng, L. & Kavanagh, K. 1999 Re-examination of the effect of a plane boundary on force and vortex shedding of a circular cylinder. *J. Wind Engng Indus. Aerodyn.* **80** (3), 263–286.

Lilly, D. K. 1992 A proposed modification of the Germano-subgrid-scale closure method. *Phys. Fluids* A **4** (3), 633–635.

Lowe, R. J., Rottman, J. W. & Linden, P. F. 2005 The non-Boussinesq lock-exchange problem. Part 1. Theory and experiments. *J. Fluid Mech.* **537**, 101–124.

Mao, Y. 1986 The interaction between a pipeline and an erodible bed. PhD thesis, Institute of Hydrodynamics and Hydraulic Engineering, Technical University of Denmark, Copenhagen, Denmark.

Martinuzzi, R. & Tropea, C. 1993 The flow around surface-mounted, prismatic obstacles placed in a fully developed channel flow. *J. Fluids Engng* **115** (1), 85–92.

Maxworthy, T., Leilich, J., Simpson, J. & Meiburg, E. 2002 The propagation of a gravity current in a linearly stratified fluid. *J. Fluid Mech.* **453**, 371–394.

Meiburg, E. & Kneller, B. 2010 Turbidity currents and their deposits. *Annu. Rev. Fluid Mech.* **42**, 135–156.

Middleton, G. V. 1993 Sediment deposition from turbidity currents. *Annu. Rev. Earth Planet. Sci.* **21** (1), 89–114.

Mittal, R. & Balachandar, S. 1995 Effect of three-dimensionality on the lift and drag of nominally two-dimensional cylinders. *Phys. Fluids* **7** (8), 1841–1865.

Munroe, J., Voegeli, C., Sutherland, B., Birman, V. & Meiburg, E. 2009 Intrusive gravity currents from finite-length locks in a uniformly stratified fluid. *J. Fluid Mech.* **635**, 245–273.

Necker, F., Härtel, C., Kleiser, L. & Meiburg, E. 2002 High-resolution simulations of particle-driven gravity currents. *Intl J. Multiphase Flow* **28** (2), 279–300.

Necker, F., Härtel, C., Kleiser, L. & Meiburg, E. 2005 Mixing and dissipation in particle-driven gravity currents. *J. Fluid Mech.* **545**, 339–372.

Niedoroda, A. W., Reed, C. W., Parsons, B. S., Breza, J., Forristall, G. Z. & Mullee, J. E. 2000 Developing engineering design criteria for mass gravity flows in deepsea slope environments. In *Proceedings of the Offshore Technology Conference*, 12069MS.

Norberg, C. 2003 Fluctuating lift on a circular cylinder: review and new measurements. *J. Fluid Struct.* **17**, 57–96.

Ooi, S. K., Constantinescu, S. G. & Weber, L. 2005 Two-dimensional large eddy simulation of lock-exchange gravity current flows. In *Proceedings of the 31st International Association Hydraulic Research Congress*, Seoul, South Korea.

Ooi, S. K., Constantinescu, S. G. & Weber, L. 2007*a* A numerical study of intrusive compositional gravity currents. *Phys. Fluids* **19** (7), 076602–076602-14.

Ooi, S. K., Constantinescu, S. G. & Weber, L. 2007*b* Two-dimensional large-eddy simulation of lock-exchange gravity current flows at high Grashof numbers. *J. Hydraul. Engng* **133** (9), 1037–1047.

Ooi, S. K., Constantinescu, S. G. & Weber, L. 2009 Numerical simulations of lock-exchange compositional gravity current. *J. Fluid Mech.* **635**, 361–388.

Pierce, C. D. 2001 Progress-variable approach for large eddy simulation of turbulent combustion. PhD thesis, Stanford University, Palo Alto, CA.

Pierce, C. D. & Moin, P. 2004 Progress-variable approach for large-eddy simulation of non-premixed turbulent combustion. *J. Fluid Mech.* **504**, 73–97.

Posdziech, O. & Grundmann, R. 2007 A systematic approach to the numerical calculation of fundamental quantities of the two-dimensional flow over a circular cylinder. *J. Fluid Struct.* **23** (3), 479–499.

Prasad, A. & Williamson, C. H. K. 1997 Three-dimensional effects in turbulent bluff-body wakes. *J. Fluid Mech.* **343**, 235–265.

Ross, S. L., Boore, D. M., Fisher, M. A., Frankel, A. D., Geist, E. L., Hudnut, K. W., Kayen, R. E., Lee, H. J., Normark, W. R. & Wong, F. L. 2004 Comments on potential geologic and seismic hazards affecting coastal Ventura County, California. *Open-File Rep.* 2004-1286. US Geological Survey.

Shin, J. O., Dalziel, S. B. & Linden, P. F. 2004 Gravity currents produced by lock exchange. *J. Fluid Mech.* **521**, 1–34.

Simpson, J. E. 1972 Effects of the lower boundary on the head of a gravity current. *J. Fluid Mech.* **53**, 759–768.

Simpson, J. E. 1997 *Gravity Currents in the Environment and the Laboratory*. Cambridge University Press.

Sumer, B. M. & Fredsøe, J. 2002 *The Mechanics of Scour in the Marine Environment*. World Scientific.

Sumer, B. M., Truelsen, C., Sichmann, T. & Fredsøe, J. 2001 Onset of scour below pipelines and self-burial. *Coast. Engng* **42** (4), 313–335.

Taniguchi, S. & Miyakoshi, K. 1990 Fluctuating fluid forces acting on a circular cylinder and interference with a plane wall. *Exp. Fluids* **9** (4), 197–204.

Thomas, L. P., Dalziel, S. B. & Marino, B. M. 2003 The structure of the head of an inertial gravity current determined by particle-tracking velocimetry. *Exp. Fluids* **34** (6), 708–716.

Whitehouse, R. 1998 *Scour at Marine Structures: A Manual for Practical Applications*. Thomas Telford.

Williamson, C. H. K. 1996 Vortex dynamics in the cylinder wake. *Annu. Rev. Fluid Mech.* **28**, 477–539.

Zdravkovich, M. M. 1985 Forces on a circular cylinder near a plane boundary. *Appl. Ocean Res.* **7** (4), 197–201.

Zdravkovich, M. M. 1997 *Flow around Circular Cylinders, Vol. 1: Fundamentals*. Oxford University Press.